A&A, 697, A92 (2025)
https://doi.org/10.1051/0004-6361/202452710

Astronomy & Astrophysics

CHANCES, the Chilean Cluster Galaxy Evolution Survey: Selection and initial characterisation of clusters and superclusters

Cristóbal Sifón[1,⋆], Alexis Finoguenov[2], Christopher P. Haines[3,33], Yara Jaffé[4,33], B. M. Amrutha[3], Ricardo Demarco[5], E. V. R. Lima[6], Ciria Lima-Dias[7,8], Hugo Méndez-Hernández[7,8,33], Paola Merluzzi[9], Antonela Monachesi[7], Gabriel S. M. Teixeira[10], Nicolas Tejos[1], F. Almeida-Fernandes[6,11], Pablo Araya-Araya[6], Maria Argudo-Fernández[12,13], Raúl Baier-Soto[4,33], Lawrence E. Bilton[14,4,1,15], C. R. Bom[10], Juan Pablo Calderón[16,17,18], Letizia P. Cassarà[19], Johan Comparat[20], H. M. Courtois[21], Giuseppe D'Ago[22], Alexandra Dupuy[23], Alexander Fritz[24], Rodrigo F. Haack[17,18], Fabio R. Herpich[25], E. Ibar[14,33], Ulrike Kuchner[26], Ivan Lacerna[3], Amanda R. Lopes[17,18], Sebastian Lopez[27], Elismar Lösch[6], Sean McGee[28], C. Mendes de Oliveira[6], Lorenzo Morelli[3], Alessia Moretti[29], Diego Pallero[4,33], Franco Piraino-Cerda[4,33], Emanuela Pompei[30], U. Rescigno[3], Analía V. Smith Castelli[17,18], Rory Smith[4,33], Laerte Sodré Jr[6], and Elmo Tempel[31,32]

(Affiliations can be found after the references)

Received 22 October 2024 / Accepted 26 March 2025

ABSTRACT

CHANCES, the CHileAN Cluster galaxy Evolution Survey, will study the evolution of galaxies in and around 100 massive galaxy clusters from the local Universe out to $z = 0.45$, and two superclusters at $z \sim 0.05$ that contain roughly 25 Abell clusters each. CHANCES will use the new 4MOST Spectroscopic Survey Facility on the VISTA 4m telescope to obtain spectra for ~500 000 galaxies with magnitudes $r_{\rm AB} < 20.4$, providing comprehensive spectroscopic coverage of each cluster out to $5r_{200}$. Its wide and deep scope will trace massive and dwarf galaxies from the surrounding filaments and groups to the cores of galaxy clusters. This will enable the study of galaxy preprocessing and of the role of the evolving environment on galaxy evolution. In this paper, we present and characterise the sample of clusters and superclusters to be targeted by CHANCES. We used literature catalogues based on X-ray emission and the Sunyaev–Zel'dovich effect to define the cluster sample in a homogeneous way, with attention to cluster mass and redshift, as well as the availability of ancillary data. We calibrated literature mass estimates from various surveys against each other and provide an initial mass estimate for each cluster, which we used to define the radial extent of the 4MOST coverage. We also present an initial assessment of the structure surrounding these clusters based on the redMaPPer red-sequence algorithm as a preview of some of the science CHANCES will enable.

Key words. galaxies: clusters: general – galaxies: distances and redshifts – galaxies: evolution – large-scale structure of Universe

1. Introduction

Understanding what drives the evolution of galaxies and determines whether they end up as star-forming spirals or quiescent early-type galaxies remains a fundamental task within astrophysics. While most isolated galaxies remain gas-rich star-forming spirals to the present day, the bulk of galaxies within massive clusters has lost their gas and transformed into quiescent early-type galaxies (Wilman et al. 2009). Internal energetic mechanisms and external environmental processes are both expected to play major roles in the transformation of galaxies. The former may include gravitational instabilities, supernovae, stellar winds, or feedback from the central supermassive black hole. The latter can include gravitational processes, such as tidal stripping by the cluster halo and galaxy-galaxy interactions (e.g. Natarajan et al. 2002; Gnedin 2003; Smith et al. 2016, 2022; Tollet et al. 2017), and hydrodynamical processes due to the hot intracluster medium (ICM), such as gas heating or ram-pressure stripping (e.g. Gunn & Gott 1972; Treu et al. 2003; Ebeling et al. 2014; Brown et al. 2017; Quilis et al. 2017; Kulier et al. 2023) (for a review of these various effects, we refer to Boselli et al. 2022, and for a review that focused on environment-related scenarios, we refer to Alberts & Noble 2022).

It is now well established that a significant fraction of this transformation takes place not inside the clusters themselves, but in the surrounding filamentary large-scale structure out to at least $5r_{200}$. This is evidenced by the reduced level of star formation and the lower fraction of star-forming galaxies at large cluster-centric radii ($2{-}5r_{200}$) compared to coeval field galaxy populations (Hou et al. 2014; Haines et al. 2015; Lopes et al. 2024; de Vos et al. 2024). This shortfall of star-forming galaxies at large cluster-centric radii was interpreted as evidence that star-forming galaxies are at least partially quenched within galaxy groups (Zabludoff et al. 1996) before they become part of the clusters. This interpretation is supported by recent studies identifying galaxy groups in the infall regions of clusters. For instance, the fraction of star-forming galaxies within these groups is lower than was seen among other galaxies at the same cluster-centric distance (Bianconi et al. 2018; Lopes et al. 2024) and lower than for galaxies in groups that are not associated with more massive clusters (e.g. Montaguth et al. 2025). This cumulative effect of processes outside of the cluster is known as preprocessing of galaxies (Fujita 2004) and is also a topic of increased investigation in hydrodynamical simulations (e.g. Bahé et al. 2013, 2019; Pallero et al. 2022; Sifón & Han 2024).

[⋆] Corresponding author.

Beyond groups and clusters, intermediate-density environments of the cosmic web (filaments and sheets) may play an equally important role in galaxy evolution. The cosmic web dynamically impacts about half of all galaxies that fall into clusters (Cautun et al. 2014; Kuchner et al. 2022) and might cause gas accretion, secondary infall, and disk re-formation, but also gas stripping and shock heating, which suppress star formation (Martínez et al. 2016; Hasan et al. 2023). Galaxies in filament cores are redder, more massive, and tend to be elliptical, and they have lower star formation rates and higher metallicities (Donnan et al. 2022). Our model of galaxy quenching is consequently changing to account for the physical processes and the time spent in filaments, walls, and groups. We currently do not know whether these observations are solely a consequence of the relations with local density (e.g. morphology-density and star formation-density relations) or if the physical processes in cosmic filaments cause the effects we observe (O'Kane et al. 2024; Raj et al. 2024).

The cosmic evolution of star formation in and around clusters provides another key piece to constrain the timescales of galaxy transformation (Haines et al. 2013; Stroe et al. 2017; Kesebonye et al. 2023). The relevance of preprocessing for the evolution of present-day cluster galaxies is a consequence of both the late assembly of massive clusters (they have accreted half their mass and galaxy populations since $z \sim 0.5$) and the fact that a significant fraction of this accreted material is in the form of galaxy groups (McGee et al. 2009). Haines et al. (2018) showed that massive clusters contain a wealth of X-ray galaxy groups at distances $\sim r_{200}$, whose accretion can explain half of the expected mass-growth rate of clusters at late epochs.

CHANCES[1], the CHileAN Cluster galaxy Evolution Survey (Haines et al. 2023), is a 4MOST Community Survey (de Jong et al. 2019) designed to uncover the relation between the evolution of galaxies and hierarchical structure formation as it occurs through deep and wide multi-object spectroscopy of galaxy clusters and their surroundings. During its five-year survey, CHANCES will target ~500 000 cluster galaxies out to $5r_{200}$. This is approximately the distance at which environmental effects acting on infalling galaxies are expected to be sufficiently strong to start removing the extended hot gas atmospheres of galaxies and cutting off their gas supply (Bahé et al. 2013). It is also well beyond the maximum distance of $2-3r_{200}$ that can be reached by back-splash galaxies (Mamon et al. 2004; Kuchner et al. 2022; Pizzardo et al. 2024). A distance of $5r_{200}$ also corresponds approximately to the turn-around radius within which matter has detached from the Hubble-Lemaître flow and is gravitationally bounded to collapse (e.g. Bertschinger 1985; Rines & Diaferio 2006). In combination with other multi-wavelength surveys, CHANCES will capture all relevant environments in and around massive clusters, including filaments and groups, to determine the prevalence of preprocessing. This will provide a comprehensive view of the evolution of galaxies and the growth of massive clusters over the past 5 Gyr. A complementary survey, the WEAVE Wide-Field Cluster Survey (Jin et al. 2024), will be performed in the northern hemisphere with the WEAVE multi-fibre spectrograph on the *William Herschel* Telescope, characterising environmentally driven galaxy evolution with a breadth and depth comparable to those of CHANCES.

In this paper, we present the cluster selection for CHANCES (Sect. 2). We then discuss a uniform calibration of cluster masses based on literature estimates that we used to define the radial extent of the 4MOST coverage (Sect. 3). We also provide an initial evaluation of the infalling structures surrounding these clusters using a photometric cluster catalogue (Sect. 4). We conclude with a summary and final remarks (Sect. 5). The CHANCES target selection and observational setup will be described in more detail in Haines et al. (in prep.) and other forthcoming papers.

Throughout this paper, M_Δ (where $\Delta \in \{200, 500\}$) refers to the mass within r_Δ, corresponding to the radius enclosing a density Δ times the critical matter density of the Universe at each redshift. We assumed a flat ΛCDM cosmology with cosmological parameters equal to the central values inferred by Planck Collaboration VI (2020), the most relevant of which are the current expansion rate, $H_0 = 67.4\,\mathrm{km\,s^{-1}\,Mpc^{-1}}$, and the present-day matter density parameter, $\Omega_\mathrm{m} = 0.315$.

2. Survey design

The 4MOST Spectroscopic Survey Facility is a multi-fibre spectrograph about to be installed on the VISTA 4m telescope at Paranal Observatory in Chile. It is equipped with 2436 science fibres, 1624 of which feed two low-resolution spectrographs with $R \equiv \lambda/\Delta\lambda = 6500$, and 812 fibres feed a single high-resolution spectrograph with $R = 20\,000$. Fibres can be positioned across a field of view with a diameter of 2.5° (de Jong et al. 2016, 2022). 4MOST will simultaneously carry out 18 public spectroscopic surveys over its first five years of science operations, sharing the focal plane among the surveys in every observation to maximise efficiency (de Jong et al. 2019; Tempel et al. 2020a,b).

With the 4MOST survey structure, we devised a strategy to study the evolution of galaxies in and around clusters by combining a unique breadth and depth. In order to efficiently span both stellar mass and lookback times, we split the CHANCES cluster survey into a Low-z subsurvey that includes clusters and superclusters at $z < 0.07$ and down to $M_{200} \sim 10^{14}\,\mathrm{M}_\odot$ (Sect. 2.1), and an Evolution subsurvey that consists of massive ($M_{200} > 5 \times 10^{14}\,\mathrm{M}_\odot$) clusters over $0.07 < z < 0.45$ (Sect. 2.2). We refer to these two collectively as the CHANCES cluster surveys. Combined, they make CHANCES a survey with continuous coverage of massive clusters from the present day to $z = 0.45$, over the past 4.8 Gyr of cosmic time. The redshift limit of 0.45 was chosen as a compromise between maximising the redshift extent and minimising the stellar mass limit that can be achieved in the available observing time, while taking advantage of available spectroscopy (Haines et al., in prep.). In addition, CHANCES includes a novel survey of the circumgalactic medium (CGM) of cluster galaxies (CHANCES-CGM) that we briefly describe in Sect. 2.3. Because of the 4MOST observing strategy, we restrict CHANCES targets to declinations $-80° < \delta < +5°$. We also exclude clusters with Galactic latitudes $|b| < 20°$.

By covering clusters out to $5r_{200}$, CHANCES will observe, in addition to the nominal cluster list, roughly ten times as many infalling systems with masses reaching about an order of magnitude lower than the main system (see Sect. 4.1). Thus, CHANCES will provide an unprecedented view of environment-driven galaxy evolution not only as a function of stellar mass, but also of the masses of the main clusters and infalling groups. At a given cluster mass, we will also control for the large-scale cluster environment by assessing the impact of residing in a main cluster or in (or near) an infalling system such as a group or filament.

The primary requirement for a cluster to be included in CHANCES is the availability of photometry from the Dark Energy Camera Legacy Survey (DECaLS, Dey et al. 2019) data release 10 (LSDR10), which ensures accurate astrometry and

---

[1] `https://chances.uda.cl/`

photometry over our entire survey. We make one exception with the Antlia cluster (Abell S636, $z = 0.0087$, which is part of the Low-z subsurvey; Lima-Dias et al., in prep.), which is not within the LSDR10 coverage. This extremely nearby system has full coverage from the S-PLUS survey, which provides photometry in 12 narrow bands across the optical wavelength range (Mendes de Oliveira et al. 2019). Target selection in the Antlia field relies on photometric redshifts based on S-PLUS photometry (Lima et al. 2022).

For both the Low-z (including the superclusters) and Evolution subsurveys, we will target galaxies down to an r-band magnitude of 20.4. We estimate stellar masses for galaxies in Low-z clusters using the $g - i$ colour-stellar mass relation of the Taylor et al. (2011) relation. For galaxies in Evolution clusters, we do this by fitting the spectral energy distributions from the Bruzual & Charlot (2003) library and assuming a Chabrier (2003) initial mass function using the FAST++ library[2] (Kriek et al. 2009). This translates into stellar mass limits of $m_\star = 10^{8.5}\,\mathrm{M}_\odot$ and $m_\star = 10^{10}\,\mathrm{M}_\odot$, respectively[3]. The selection of target galaxies is based on photometric redshifts from LSDR10, and for a subsample of the Low-z subsurvey for which S-PLUS data are available, it is based on S-PLUS photometric redshifts, with stellar masses derived from the same photometry. Of the 500 000 spectroscopic targets within the CHANCES cluster survey, approximately 70% will be devoted to the Low-z subsurvey, with 70% of these corresponding to individual clusters and the remaining 30% to the superclusters. This means that we will target approximately 4500 galaxies per cluster in the Low-z cluster sample and approximately 2500 galaxies per Evolution cluster. All CHANCES targets will be observed with the low-resolution spectrographs. The details will be presented by Haines et al. (in prep.) and Méndez-Hernández et al. (in prep.).

Figure 1 shows the CHANCES footprint on the sky, which covers over 1600 sq. deg. in all[4]. For visibility purposes, we set each circle to have at least a radius of 1 deg. In practice, this means that essentially all of the Evolution clusters are enlarged to this size while all Low-z cluster footprints retain their original extent of $5r_{200}$. We describe the r_{200} estimates in Sect. 3. We also show several multi-wavelength surveys of interest: the Simons Observatory Large-Aperture Telescope (SO-LAT) survey (Ade et al. 2019, $-60° \lesssim \delta \lesssim +20°$), the Cerro Chajnantor Atacama Telescope (CCAT) Wide-Field Survey (WFS, CCAT-Prime Collaboration 2023, $-61° \leq \delta \leq +18°$), and the Vera C. Rubin Observatory Legacy Survey of Space and Time (LSST, Ivezić et al. 2019, $-60° \lesssim \delta \lesssim +2°$), as well as the German half of the eROSITA all-sky survey, which covers Galactic longitudes $l > 180°$ (Merloni et al. 2024). In addition to its main science goals, CHANCES will therefore also enable unique cluster and galaxy science in synergy with a rich array of multi-wavelength data.

2.1. CHANCES Low-z subsurvey

The CHANCES Low-z subsurvey is designed to target 50 clusters at $z \leq 0.07$. In addition, it will cover large regions within the Shapley and Horologium-Reticulum superclusters that each contain a large number of clusters within a rich cosmic web.

2.1.1. Galaxy cluster sample

The Low-z subsurvey includes clusters selected from the All-Sky X-ray Extended Source (AXES) catalogue (Damsted et al. 2024; Khalil et al. 2024), the Wide-field Nearby Galaxy cluster Survey (WINGS, Fasano et al. 2006), and a number of clusters selected individually based on their known properties or available datasets. We describe each subset below.

AXES is a reanalysis of the ROSAT All-Sky Survey (RASS) data in which X-ray emission from extended sources was detected on scales of 12−24 arcmin via wavelet decomposition (Damsted et al. 2024). It is complete in the extragalactic area down to a flux of $1 \times 10^{-12}\,\mathrm{ergs\,s^{-1}\,cm^{-2}}$. AXES sources have been validated against a group catalogue based on Sloan Digital Sky Survey (SDSS) data (Tempel et al. 2017) by Damsted et al. (2024), against the Two-Micron All Sky Survey (2MASS) Redshift Survey (2MRS) spectroscopic galaxy group catalogue (Tempel et al. 2018) by Khalil et al. (2024), and against a cluster catalogue constructed with the redMaPPer cluster red-sequence finder applied to LSDR10 by Finoguenov et al. (in prep.). We use the latter two cross-matched catalogues in this work and refer to them as AXES-2MRS and AXES-LEGACY, respectively. The scales probed by AXES correspond to about r_{500}–r_{200} at $z < 0.04$, which offers the unique advantage of using the scales at which cluster behaviour is best understood. However, beyond $z = 0.04$, these angular scales extend beyond r_{200}, and AXES sources become affected by blending. In addition, the feedback processes on low-mass clusters lead to baryonic lifting, which results in additional flux compared to estimates based on L_{500} (the X-ray luminosity within r_{500}). This means that the scales used in the AXES analyses are best suited to cluster characterisation at $z < 0.04$ (Khalil et al. 2024; Damsted et al. 2024). Conversely, below $z = 0.01$, the scales used by AXES only probe cluster cores, which changes the selection function[5]. In any case, there are few massive clusters at these low redshifts, and most of them have good auxiliary information. In addition, to ensure low contamination, we only considered AXES clusters with at least five member galaxies (spectroscopic in the case of AXES-2MRS and photometric in the case of AXES-LEGACY). Therefore, we used the subset of AXES-2MRS with at least five spectroscopic member galaxies as our parent sample at $z < 0.04$.

WINGS (Fasano et al. 2006), together with its extension OmegaWINGS (Gullieuszik et al. 2015), is a multi-wavelength imaging and spectroscopic survey of 77 galaxy clusters at $0.04 \leq z \leq 0.07$ (perfectly complementing the redshift coverage of AXES-2MRS) that were selected from cluster catalogues constructed from the RASS. We included WINGS as one of the CHANCES Low-z parent catalogues because of the wealth of optical spectroscopy that is already available in the central regions of these clusters (Cava et al. 2009; Moretti et al. 2014, 2017). The 4MOST observations will complement the available data to reach the CHANCES specifications.

With these two parent samples, we designed the Low-z subsurvey to cover an order of magnitude in mass at redshifts $z < 0.07$, sampling known clusters with an essentially uniform distribution in mass at $M_{200} \gtrsim 10^{14}\,\mathrm{M}_\odot$, plus a few well-known lower-mass systems. The Low-z cluster sample is listed in Table A.1.

---

[2] `https://github.com/cschreib/fastpp`

[3] We verified that the Taylor et al. (2011) relation applied to Evolution targets gives consistent results.

[4] This only refers to the cluster subsurveys described in Sects. 2.1 and 2.2, that is, it does not include the CHANCES-CGM subsurvey that is briefly described in Sect. 2.3.

[5] The lowest-redshift cluster in AXES-2MRS has $z = 0.0015$ and $M_{200} = 1.1 \times 10^{13}\,\mathrm{M}_\odot$.

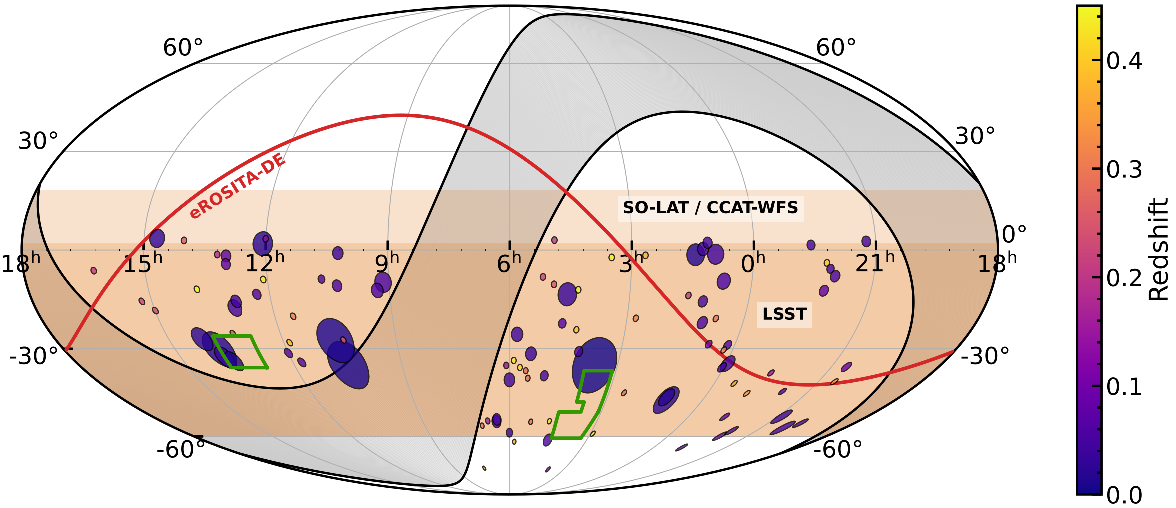

Fig. 1. Sky distribution of CHANCES clusters in equatorial coordinates in a Mollweide projection. The radius of each circle corresponds to the maximum between $5r_{200}$ and 1 deg (the latter set for visibility) and is colour-coded by redshift. The supercluster regions are shown with green polygons. The region below the red curve corresponds to the eROSITA-DE survey, the dark orange region shows the approximate LSST survey area, and the light orange region shows SO-LAT and CCAT-WFS (for simplicity, we draw both as delimited by $-60° \leq \delta \leq +18°$). The grey band bounded by black lines shows Galactic latitudes $|b| \leq 20°$.

2.1.2. Superclusters

The CHANCES Low-z subsurvey also includes wide regions covering two well-known superclusters: the Shapley supercluster at $z = 0.048$ (e.g. Reisenegger et al. 2000; Proust et al. 2006; Merluzzi et al. 2015; Haines et al. 2018) and the Horologium-Reticulum supercluster at $z = 0.060$ (e.g. Lucey et al. 1983; Fleenor et al. 2005, 2006). The exact regions were chosen as a compromise between the number of included member clusters and the available fibre hours for the entire survey. Spectroscopic targets are selected using the same magnitude limit as the Low-z cluster subsurvey: an r-band magnitude lower than 20.4 across the entire supercluster regions, independently of local density. This ensures a complete census of the structure within them (Haines et al., in prep.).

The CHANCES coverage of the Shapley supercluster corresponds to a rectangle bounded by right ascensions $192° \leq \alpha \leq 207°$ and declinations $-36° \leq \delta \leq -26°$, containing 128 deg^2, plus the remaining area within $5r_{200}$ of Abell 3571 at the same redshift. The coverage of the Horologium-Reticulum supercluster is enclosed by the following polygon vertices[6]: [46.5, −51]; [49, −60.7]; [66, −60.7]; [66, −51]; [55, −51]; [55, −47.5]; [58.5, −47.5]; [58.5, −37]; [46.5, −37]. This polygon covers an area of 225 deg^2. The supercluster region is supplemented by the $5r_{200}$ area around Abell 3266, which marginally overlaps the supercluster in the south-eastern corner, also at the supercluster redshift. Other Low-z clusters overlapping the superclusters in the sky but not in redshift are Abell 3565 and Abell 3574 with Shapley and Fornax with Horologium-Reticulum. In the regions in common with the latter clusters, we include in our target catalogues galaxies with photometric redshifts that match any of the overlapping systems. However, for faint galaxies approaching our magnitude limit, the photometric redshift errors are larger than the redshift difference between the clusters and superclusters. This means in practice that faint targets are common to both systems. This overlap will, in any case, ensure a high completeness for the clusters and superclusters (Méndez-Hernández et al., in prep.). The supercluster survey regions are shown in Fig. 1.

2.2. CHANCES Evolution subsurvey

As part of the CHANCES Evolution subsurvey, we will target 50 of the most massive galaxy clusters distributed evenly over $0.07 < z < 0.45$. The Evolution sample is primarily selected from the second Planck catalogue of Sunyaev–Zel'dovich (SZ) sources (PSZ2; Planck Collaboration XXVII 2016), which provides a homogeneous all-sky sample of massive clusters over this redshift range and is not noticeably biased by dynamical state (Planck Collaboration XXVII 2016; Andrade-Santos et al. 2017; Rossetti et al. 2017). We selected the 10 most massive PSZ2 clusters with available DESI Legacy Imaging Survey DR10 grz imaging and photometric redshifts out to $5r_{200}$ in each of five linearly spaced intervals over $0.07 < z < 0.45$. This binned selection ensures continuity with the Low-z subsurvey: There are 8 Evolution clusters at $0.07 < z < 0.10$. It also translates to a minimum mass $M_{200} = 7 \times 10^{14}\, M_\odot$ at $z > 0.2$, while at lower redshifts, the mass limit is progressively reduced to account for the smaller available volume. This selection is similar to the selection that was used for cluster cosmology by Planck Collaboration XXIV (2016), and the larger extent of more massive clusters allows an efficient use 4MOST at $z > 0.3$. Most of the CHANCES Evolution cluster sample is covered by the CHEX-MATE XMM Heritage programme (CHEX-MATE Collaboration 2021), which provides high-quality X-ray data that are suitable for characterising the ICM and mass distributions of each CHANCES cluster.

The only cluster in the Evolution subsurvey that is not matched to any PSZ2 source is MACS J0329.7−0211 at $z = 0.45$. We include it in CHANCES to take advantage of the extensive available spectroscopy from the CLASH-VLT survey (Girardi et al. 2024). The Evolution cluster sample is listed in Table A.2.

2.3. CHANCES CGM subsurvey

In addition to the cluster samples described above, CHANCES will offer a unique view of the CGM in and around clusters by observing ∼50 000 galaxies around ∼10 000 background quasars behind roughly 4000 unique galaxy clusters. Quasars

---

[6] These are given as $[\alpha, \delta]$ in degrees.

are selected either from optical spectroscopy (Lyke et al. 2020; Anand et al. 2021) or from X-ray imaging (Merloni et al. 2019). We require that they lie within 6 Mpc in projection from foreground clusters at $0.35 < z < 0.7$, where the Mg II line falls in the wavelength range covered by 4MOST. This experimental setup builds up from the setup that was pioneered by Lopez et al. (2008). Clusters for the CGM subsurvey are selected from a catalogue constructed by applying the redMaPPer algorithm (Rykoff et al. 2014) to the LSDR10 data (Kluge et al. 2024; see Sect. 4). The main goal of the CGM subsurvey is to establish the origin of intervening Mg II absorbers and their relation to galaxies as a function of galaxy type and both local and large-scale environment. In this manner, we will construct a detailed view of the CGM transformations that occur in dense environments and their impact on galaxy evolution, which will provide a novel complement to the CHANCES cluster survey. More details will be given in a forthcoming paper.

3. Cluster mass estimates

As described in the previous section, we selected clusters homogeneously based on mass proxies from X-rays (Low-z) and the thermal SZ effect (evolution). However, we used masses from a variety of sources in an attempt to obtain the best r_{200} estimate for each cluster while still maintaining some homogeneity in the mass estimates. To this end, we cross-matched our cluster samples with several catalogues that provide masses with different techniques, as summarised in Tables 1 and 2 (explained below). Because we combined several cluster surveys, it was important to homogenise their mass estimates to provide uniformity. We emphasise here that the goal of this exercise was not to obtain accurate and precise mass estimates based on all the available data for each cluster, but to establish a preliminary mass scale from which to obtain an estimate of r_{200}, which was used to define the extent of our target galaxy catalogues.

We retrieved mass estimates from various surveys and applied a normalisation factor to each one to ensure statistical consistency. Because different assumptions were made to estimate the masses in each of the catalogues, this is preferable to combining masses from different catalogues. In order to estimate the normalisation factors, we matched clusters across catalogues with a 5′ matching radius and a maximum redshift difference of 10%. The former matches the PSZ2 beam size and is small compared to the extent of Low-z clusters, while the latter allows photometric redshift errors, and we tested that more stringent matching criteria do not change the outcome. We show examples of cross-matched catalogues and the resulting mass normalisations in Fig. 2, and we summarise the normalisations we applied to each external catalogue in Tables 1 and 2. We fit the normalisations, a, by fitting a linear relation using a maximum likelihood procedure including intrinsic scatter,

$$\mathcal{L} = \prod_i \frac{1}{\sqrt{2\pi} w_i} \exp\left(-\frac{[\log M_{200}^{y,i} - (a + \log M_{200}^{x,i})]^2}{2 w_i^2} \right). \qquad (1)$$

The weights w_i account for the uncertainties in the two quantities δx_i and δy_i and for the intrinsic scatter, $\sigma_{\rm int}$,

$$w_i^2 = (\delta x_i)^2 + (\delta y_i)^2 + \sigma_{\rm int}^2. \qquad (2)$$

The latter holds for a linear relation (e.g. Hoekstra et al. 2012). The inclusion of intrinsic scatter as a free parameter alleviates the effect of unrealistically small reported uncertainties, such as those in the left panel of Fig. 2, which only include the statistical uncertainties and not the uncertainties from the pressure profile fit or the scaling relations.

In order to assign a mass to each cluster, we preferred the weak lensing masses at all redshifts. When no weak lensing masses were available, we preferred AXES at low redshifts for the reasons given above, followed by SZ-based masses because they are more stable and introduce less scatter than traditional X-ray masses (e.g. Rozo et al. 2014; Kugel et al. 2025). Within the remaining catalogues, we preferred those containing more CHANCES clusters for homogeneity while prioritising WINGS over MCXC at low redshift because its selection is similar to that of CHANCES. As shown in Fig. 2, the exact choice introduces a 20–30% scatter in mass, which translates into a $\lesssim$10% scatter in r_{200}.

As a reference scale for the Low-z subsurvey masses, we therefore used the weak lensing mass estimates from MENeaCS

Table 1. Mass sources for the Low-z subsurvey, ordered by priority.

Survey	(1) Normalisation	(2) No. of clusters	(3) Source for
MENeaCS [(a)]	1	5	5
AXES-2MRS [(b)]	0.86	21	11
AXES-LEGACY [(c)]	0.86	36	1
ACT-DR5 [(d)]	1	5	2
SPT-ECS [(e)]	1	1	0
SPT-SZ [(f)]	1	2	1
WINGS [(g)]	0.76	18	13
MCXC [(h)]	1.37	43	14
PSZ2 [(i)]	1.09	27	2
CODEX [(j)]	0.69	34	1

Notes. The columns list (1) the correction factor applied to masses provided by the survey, according to the comparison described in Sect. 3; (2) the total number of CHANCES clusters in each catalogue; and (3) the number of clusters with CHANCES mass estimates from each source. [(a)]Herbonnet et al. (2020). [(b)]Khalil et al. (2024). Used only as source for clusters at $z \leq 0.04$. [(c)]Finoguenov et al. (in prep.). Used only for clusters at $z \leq 0.04$, except for Abell 3490 ($z = 0.069$), which is not matched in any other catalogue. [(d)]Hilton et al. (2021), [(e)]Bleem et al. (2020), [(f)]Bleem et al. (2015), [(g)]Moretti et al. (2017), [(h)]Piffaretti et al. (2011), [(i)]Planck Collaboration XXVII (2016), [(j)]Damsted et al. (2023).

Table 2. Mass sources for the Evolution sub-survey, ordered by priority.

Survey	Normalisation	No. of clusters	Source for
LoCuSS [(a)]	1	4	4
MENeaCS	1	11	8
CoMaLit [(b)]	1	25	13
ACT-DR5	1	34	14
SPT-ECS	1	14	3
SPT-SZ	1	12	2
PSZ2	1.09	49	6
CODEX	0.69	40	0
MCXC	1.37	40	0

Notes. See Table 1 for details and additional references. [(a)]Okabe & Smith (2016). Does not contain any clusters in the Low-z redshift range. [(b)]Sereno (2015).

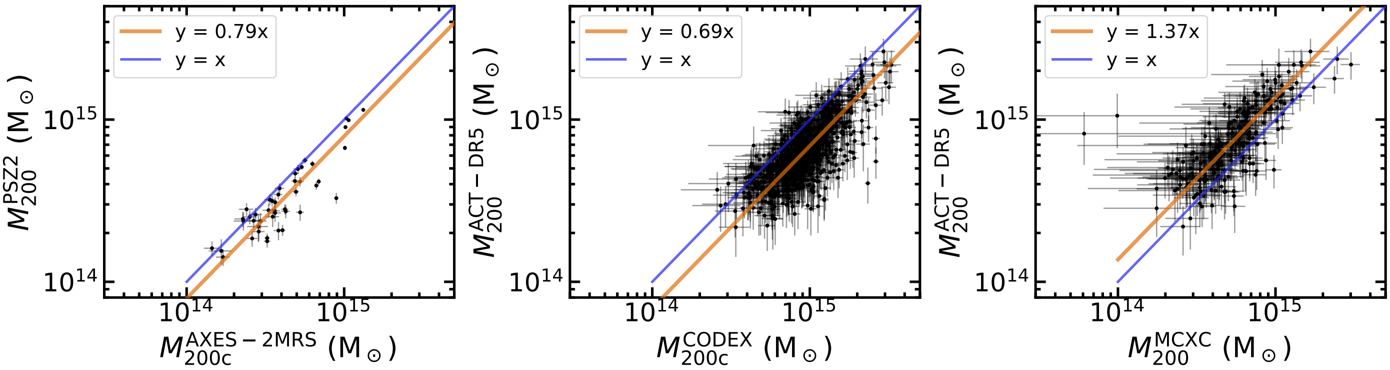

Fig. 2. Mass comparison examples. From left to right, we compare the mass estimates of PSZ2 to AXES-2MRS, ACT-DR5 to CODEX, and ACT-DR5 to MCXC. The points with error bars show all clusters in common between each pair of catalogues, regardless of whether they are part of CHANCES. Thin blue lines show $y = x$, and the thick orange lines show the maximum-likelihood estimates given in the legends. The extremely small uncertainties in PSZ2 and AXES-2MRS only consider statistical uncertainties. We account for this fact by including an intrinsic scatter term in the fits. These fits correspond to the adopted normalisations discussed in Sect. 3 and listed in Tables 1 and 2.

(Herbonnet et al. 2020), while for the Evolution subsurvey, we also used the masses derived from ACT-DR5 SZ effect mass estimates, which were normalised to match the scale of weak lensing mass estimates as described by Hilton et al. (2021)[7]. While MENeaCS masses are given as M_{200}, ACT-DR5 masses are given as M_{500}. We converted these and other mass definitions as appropriate into M_{200} using `colossus`[8] (Diemer 2018). For this, we assumed an NFW profile (Navarro et al. 1996) with the Ishiyama et al. (2021) mass-concentration relation.

We therefore defined the CHANCES mass of each CHANCES cluster following the order in Tables 1 and 2 for the Low-z and Evolution samples, respectively. In each table, the last column lists the number of clusters that derived their CHANCES mass from that catalogue, while the previous column lists the total number of CHANCES clusters in each catalogue. In the case of Low-z, this means, for instance, that all 5 clusters in MENeaCS are assigned the MENeaCS masses, and the 11 AXES-2MRS clusters with $z \leq 0.04$ that are not in MENeaCS are assigned the AXES-2MRS mass multiplied by 0.86, and so on. We only considered AXES-2MRS and AXES-LEGACY for clusters at $z \leq 0.04$, as discussed in Sect. 2.1.

When there are not enough cross-matches between a particular catalogue and the reference catalogue, we applied successive normalisations. For example, the normalisation of 0.86 for AXES-2MRS (and AXES-LEGACY) comes from the combination of $M_{200}^{\rm PSZ2} = 0.79 M_{200}^{\rm AXES-2MRS}$ (shown in the left panel of Fig. 2) and $M_{200}^{\rm ACT-DR5} = 1.09 M_{200}^{\rm PSZ2}$ (not shown). The ACT-DR5 and the two SPT catalogues were shown to be consistent with each other and with weak lensing mass estimates (Bleem et al. 2020; Hilton et al. 2021), and we therefore set all these normalisations to one.

The two outliers in the right panel of Fig. 2 are Abell 536 at $z = 0.040$ and Abell S560 at $z = 0.037$, with ACT-DR5 masses 11 and 13 times the MCXC masses, respectively. At these low redshifts, the ACT-DR5 catalogue is highly incomplete, and it is therefore expected that some clusters are up-scattered due to either statistical or intrinsic noise. This may raise concerns about using ACT-DR5 in the Low-z sample. Reassuringly, the mass estimates of the two Low-z clusters assigned ACT-DR5 masses (Abell 3667 at $z = 0.053$ and Abell 4059 at $z = 0.048$) from ACT-DR5, PSZ2, MCXC, AXES-LEGACY, and WINGS, with standard deviations of 16% and 29%, respectively. The catalogue choice therefore affects the assigned r_{200} only little (namely, 5% and 10%, respectively).

There are two exceptions to the above scheme, and both pertain to the Low-z subsurvey. The first is Abell 3395, which is a well-known merging system that also lies in close proximity to Abell 3391 (e.g. Reiprich et al. 2021; Dietl et al. 2024; Veronica et al. 2024). Abell 3395 has a mass estimate from the WINGS survey of $M_{200} = 2.9 \times 10^{15}\,{\rm M}_\odot$ (Moretti et al. 2017), while all ICM-based estimates suggest $M_{200} \sim 5 \times 10^{14}\,{\rm M}_\odot$ (Piffaretti et al. 2011; Planck Collaboration XXVII 2016; Bulbul et al. 2024; Damsted et al. 2024). Because mass estimates based on the velocity dispersion are known to be highly biased for merging clusters (as was indeed pointed out by Moretti et al. 2017), we instead chose use the PSZ2 mass for Abell 3395, $M_{200} = 5.1 \times 10^{14}\,{\rm M}_\odot$. The other exception is Abell 3490, for which we used the rescaled AXES-LEGACY mass even though it is at $z = 0.069$, because it is not matched to any other catalogue. The resulting mass estimates for each cluster and the associated r_{200} are listed in Tables A.1 and A.2.

We show the CHANCES clusters in mass–redshift space in Fig. 3. We place the sample of each subsurvey in context by comparing it to the mass and redshift distributions of clusters in PSZ2 and AXES-2MRS (Low-z, left panel) and PSZ2 and ACT-DR5 (Evolution, right panel) over the sky available to CHANCES (i.e. $\delta < +5°$, $|b| > 20°$). We removed duplicates from Fig. 3 by matching clusters as described above (a matching radius of 5′ and a redshift difference of <10%), following the priority scheme already described. That is, in the left panel, we only show as green crosses AXES-2MRS clusters that are not in CHANCES and only show as purple circles PSZ2 clusters that are neither in AXES-2MRS nor CHANCES. This is done analogously for the Evolution sample in the right panel.

CHANCES includes all of the massive nearby clusters with LSDR10 coverage in the southern hemisphere at $|b| > 20°$. The massive AXES-2MRS clusters that are not part of CHANCES all lack LSDR10 coverage in a significant fraction of their $5r_{200}$ area. The most massive of these are Abell 3526 at $z = 0.011$ and Abell 4038 at $z = 0.029$. CHANCES Low-z clusters cover the entire mass range probed by AXES and PSZ2 over $0 < z < 0.07$. With a few exceptions, in contrast, the Evolution sample specifically targets the most massive systems, although as mentioned, we enforced homogeneous coverage of the full Evolution redshift range. This continuous sampling of the most massive clus-

---

[7] That is, we used the `M500cCal` column.

[8] https://bdiemer.bitbucket.io/colossus/

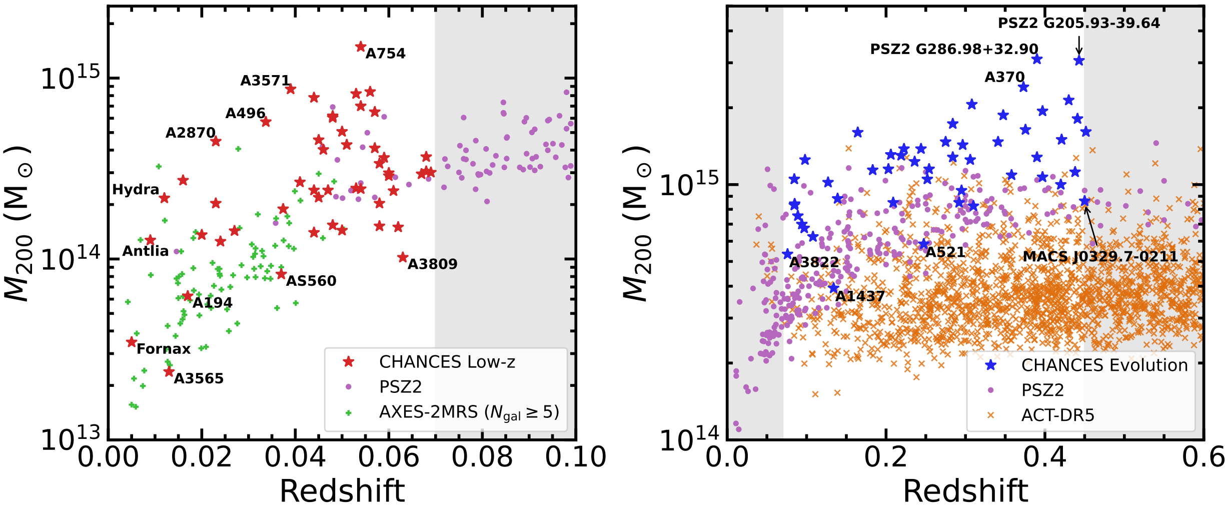

Fig. 3. CHANCES cluster samples (stars) in context. Left: Low-z subsurvey, excluding clusters in the Shapley and Horologium-Reticulum superclusters, compared with southern (Dec < +5°) clusters in AXES-2MRS (with at least five spectroscopic members) and PSZ2, also excluding clusters in the supercluster regions. Right: Evolution subsurvey, compared with southern clusters in PSZ2 and ACT-DR5. In both cases, we removed duplicate clusters by only keeping the higher-priority mass estimate (see Sect. 3), and we removed clusters with Galactic latitudes $|b| < 20°$. We give the names of the least and most massive clusters in each sample, as well as the names of some well-known clusters. In the right panel, we also highlight MACS J0329.7−0211, which is the only Evolution cluster that is not in PSZ2. The redshift range of each CHANCES subsurvey is shown with the white background. The CHANCES cluster masses correspond to those listed in Tables A.1 and A.2.

ters from $z = 0$ to $z = 0.45$ is not designed to track the evolution of clusters: It is evident that clusters in the Low-z sample are not the descendants of clusters in the Evolution sample. By targeting the entire volume around each cluster that is detached from the Hubble-Lemaître flow, we will instead determine the effect of the time of arrival on the infall patterns and its consequences on galaxy evolution. This is known as the Butcher-Oemler effect (Butcher & Oemler 1984). The superclusters then provide a natural extension by probing larger-scale environments including the full region that will become detached from the Hubble-Lemaître flow in the distant future (Dünner et al. 2006; Araya-Melo et al. 2009).

We expand upon the previous point by looking at the reconstruction of the peculiar velocities of CHANCES clusters. These peculiar velocities were derived by Dupuy & Courtois (2023) by reconstructing the large-scale density using the distances estimated by the Cosmicflows-4 project (Courtois et al. 2023). Peculiar velocities trace the location in the large-scale structure of the Universe: Generally speaking, large peculiar-velocity structures fall towards small peculiar-velocity structures. Figure 4 shows the distribution[9] of peculiar velocities of all CHANCES clusters (excluding superclusters), compared to all Abell clusters (Abell et al. 1989) with known redshifts[10] as well as the ROSAT-ESO Flux Limited X-ray (REFLEX) cluster sample (Böhringer et al. 2004). The peculiar velocities of most CHANCES clusters are lower than 500 km s^{-1}. While a few have somewhat higher peculiar velocities, the distribution is much more skewed to lower values than the other samples. This suggests CHANCES clusters are preferentially local attractors. These peculiar-velocity estimates offer yet another aspect whose impact on galaxy evolution will be uniquely assessed by CHANCES.

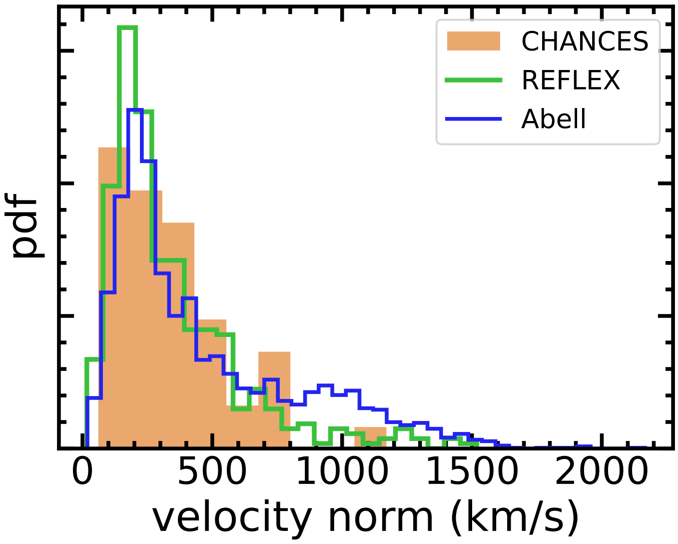

Fig. 4. Three-dimensional peculiar velocity norm distribution of CHANCES clusters, compared to all Abell and REFLEX clusters with known redshifts. These have been reconstructed by Dupuy & Courtois (2023) from distances estimated by Cosmicflows-4 (Courtois et al. 2023). Bin sizes were chosen following Knuth (2006).

4. Cluster environments: A sneak peek

4.1. A preliminary census of infalling structures around CHANCES clusters

One of the primary goals of CHANCES is to study the preprocessing of galaxies prior to cluster infall. It is thus important to characterise not only the main clusters, but also the surrounding structures. As a proof of concept, we explored

---

[9] We defined the bin widths using the rule described by Knuth (2006), which optimises the bin size of a piecewise-constant probability distribution in a Bayesian framework. We used the implementation in `astropy.visualization`.

[10] As listed in the NASA/IPAC Extragalactic Database, `http://ned.ipac.caltech.edu/`

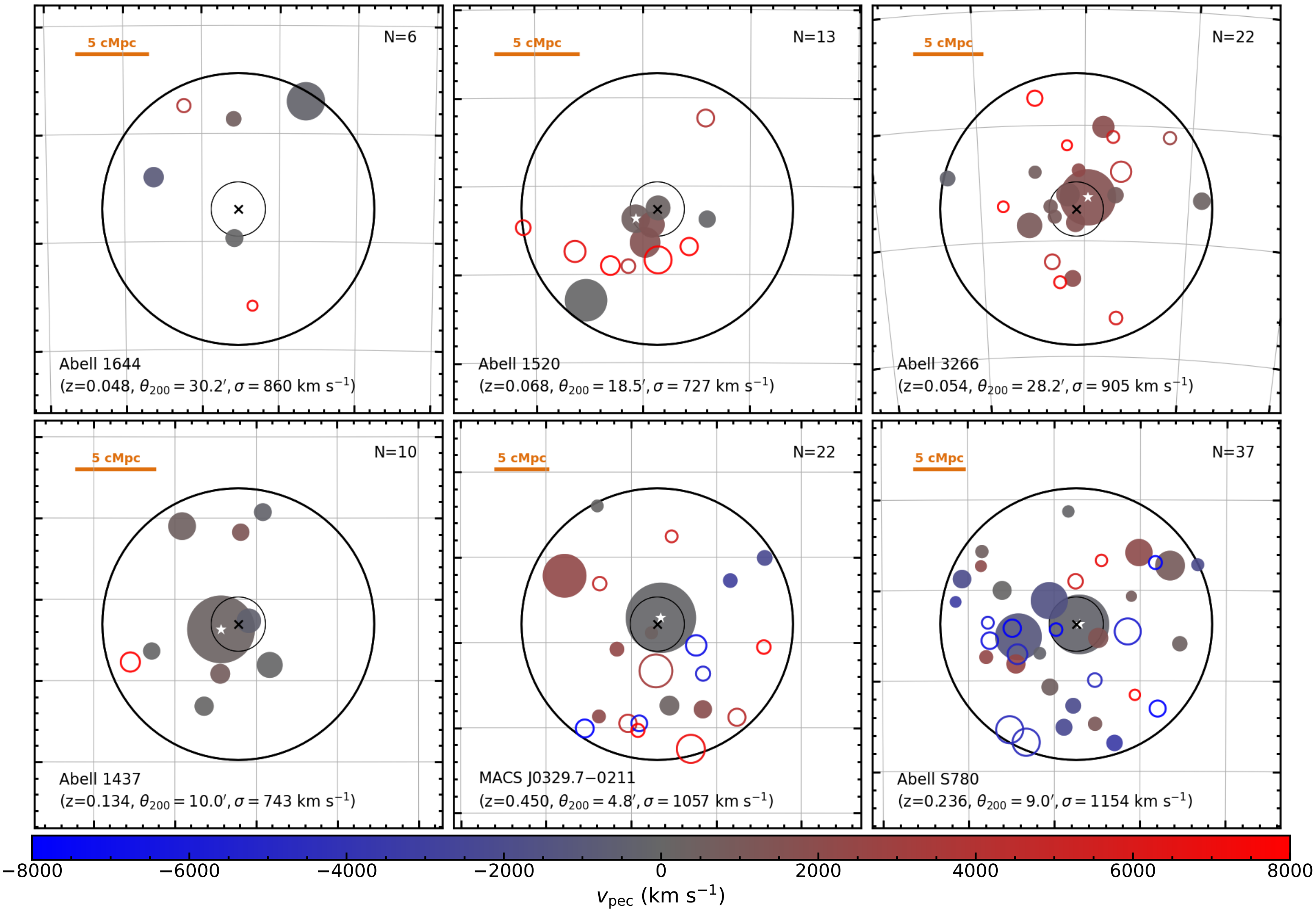

Fig. 5. Infalling structures in example CHANCES Low-z (top) and Evolution (bottom) clusters as traced by associations of red galaxies identified with redMaPPer within 8000 km s^{-1} of the nominal redshift of each CHANCES cluster. The filled circles correspond to redMaPPer groups with velocities within three times the CHANCES velocity dispersion. For each subsurvey, we show a cluster with a small (left), typical (middle), and large (right) number of redMaPPer groups around them. The concentric black cross and empty thin and thick circles mark the centre of each CHANCES cluster, r_{200}, and $5r_{200}$, respectively. The coloured circle sizes correspond to the r_{200} of each group based on its richness. The colour scale shows the peculiar velocity with respect to the main cluster. When present, the redMaPPer system associated with the main CHANCES cluster is shown with a white star. In the bottom of each panel, we list the redshift, angular size corresponding to r_{200}, and richness-derived velocity dispersion of each cluster. The numbers in the top right corners correspond to the number of redMaPPer groups, and the orange bars in the top left corners indicate 5 comoving Mpc at the redshift of each cluster.

the network of groups[11] around CHANCES clusters using the redMaPPer (Rykoff et al. 2014) group catalogue generated using the LSDR10. This catalogue was constructed by Kluge et al. (2024) to provide targets for the 4MOST eROSITA Galaxy Cluster Redshift Survey (Finoguenov et al. 2019) following the strategy described by Clerc et al. (2020). redMaPPer identifies associations of red galaxies and calculates the richness, λ, as the total membership probability across all galaxies within a richness-dependent cluster radius that is about 1 Mpc. The cluster centre is chosen as the location of the most likely central galaxy based on galaxy position, magnitude, and colour, as described by Rykoff et al. (2014). By construction, the redMaPPer catalogue does not contain systems lacking a developed red sequence. This selection effect only impacts low-mass systems, and overcoming it requires the spectroscopic completeness that CHANCES will provide. We describe all of the redMaPPer group properties used in this demonstration (namely redshifts z and their uncertainties δz, peculiar velocities $v_{\rm pec}$, masses M_{200}, and velocity dispersions σ_v) in Appendix B. For the purpose of this demonstration, we also calculated the one-dimensional velocity dispersion of each CHANCES cluster given M_{200}, using the relation by Munari et al. (2013). We call this velocity dispersion $\sigma_{\rm main}$.

We considered all redMaPPer groups within $5r_{200}$ of each CHANCES clusters and with $|v_{\rm pec}| < 8000\,{\rm km\,s^{-1}}$. Figure 5 shows the redMaPPer groups thus selected around example Low-z and Evolution clusters. There are a total 1406 redMaPPer groups thus selected, which is an average 13.5 redMaPPer groups within $5r_{200}$ of each CHANCES cluster. We then identified the most massive redMaPPer group within the nominal CHANCES r_{200} (see Tables A.1 and A.2) as the CHANCES cluster itself. Automatic cluster finding is notoriously difficult at very low redshift, where the mean separation between galaxies is several arcminutes on the sky. The LSDR10 data in addition lack u-band data, which is critical for photometric redshift estimation at $z < 0.1$, where it is needed to detect the 4000 Å break and to identify star-forming contaminants (Rozo et al. 2016). We

---

[11] Traditionally, the division between the terms cluster and group is set by a mass threshold, typically around $10^{14}\,{\rm M_\odot}$. In an attempt to reduce confusion and redundancy, we use both terms hierarchically in this section: CHANCES clusters are surrounded by redMaPPer groups, regardless of mass.

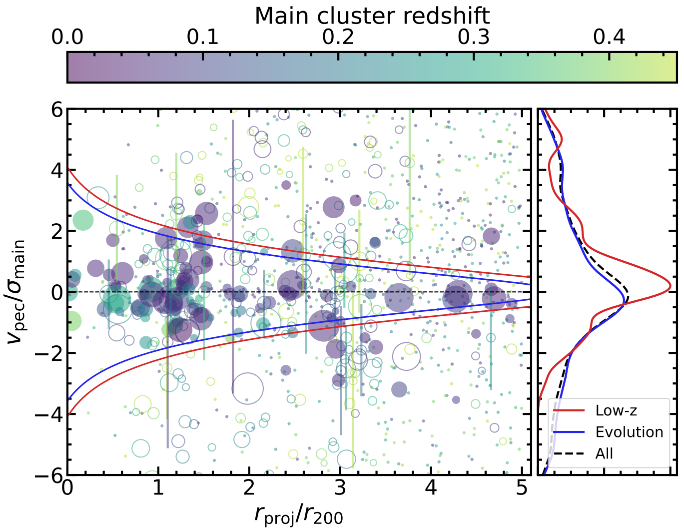

Fig. 6. Line-of-sight velocity vs. projected distance of redMaPPer groups around all CHANCES clusters, normalised by the velocity dispersion and r_{200} of each CHANCES cluster, respectively. Each circle shows a redMaPPer group with a spectroscopic redshift, has a radius proportional to the group richness-derived r_{200} in units of each CHANCES cluster r_{200}, and is colour-coded by redshift. The filled and open circles show clusters with uncertainties $\delta v_{\rm pec}$ smaller and larger than $\sigma_{\rm main}$, respectively. We show uncertainties for a random 10% of the latter for illustration; the uncertainties for filled circles are about the circle size and are not shown. The small points show groups with photometric redshifts. redMaPPer groups corresponding to the main CHANCES cluster are excluded from this plot. The red and blue lines in the main panel show the escape velocities for typical Low-z and Evolution clusters; groups with higher peculiar velocities are expected to be unbound from the respective CHANCES cluster. The right panel shows kernel density estimates of the peculiar-velocity distributions of redMaPPer groups with spectroscopic redshifts only (filled and empty circles in the main panel), using a Gaussian kernel with a width of 0.2 for the Low-z (red) and Evolution (blue) samples, and the combined distribution (dashed black).

assigned a redMaPPer group with the main CHANCES cluster in 30 Low-z clusters, all at $z > 0.037$, while the rest (all at $z < 0.048$) have no redMaPPer matches within r_{200}. One such example is Abell 1644, which we show in the top left panel of Fig. 5. Some clusters, however, may be matched to the wrong main cluster, such as in the case of Abell 1520 in the top centre panel of Fig. 5. All Evolution clusters have a redMaPPer match, except for RXJ 1347.5−1144, which is not within the LSDR10 redMaPPer footprint because it is covered in *giz*, but not in *r*-band. As expected, some CHANCES clusters contain a wealth of infalling groups, although this is not apparent in others from the redMaPPer catalogue. This may be due either to incompleteness in the redMaPPer catalogue (e.g. because these low-mass systems might not contain a red sequence) or because some CHANCES clusters really reside in regions that are devoid of significant galaxy overdensities. This question can only be answered by the high spectroscopic completeness provided by CHANCES.

We now describe the statistical properties of the redMaPPer sample and its relation to the CHANCES clusters. In Fig. 6 we show the line-of-sight velocity against the projected cluster-centric distance (this is generally referred to as a phase-space diagram) for the redMaPPer groups that surround the CHANCES clusters. Phase-space diagrams are commonly used to infer the infall history of galaxy populations within clusters (e.g. Oman et al. 2013; Muzzin et al. 2014; Haines et al. 2015; Jaffé et al. 2015). As with galaxies, the phase-space diagram of infalling groups reveals details of their infall history (e.g. Jaffé et al. 2016; Einasto et al. 2018; Haines et al. 2018; Piraino-Cerda et al. 2024). Each data point in Fig. 6 is a redMaPPer group near a CHANCES cluster. The large number of groups with either spectroscopic redshifts with large uncertainties or photometric redshifts highlight the rich structure potentially available for CHANCES to uncover. The main CHANCES clusters were excluded from Fig. 6 following the associations described above. However, some redMaPPer groups are located right at the CHANCES cluster centres. These are cases where the simple association above clearly failed, possibly due to the fragmentation of the system by redMaPPer (e.g. Abell 1520 and Abell 1437 in Fig. 5). We treat these failures as nuisance in the context of the proof of concept presented here.

We also show in Fig. 6 the escape velocity profiles for typical Low-z and Evolution clusters (with $M_{200} = \{3, 10\} \times 10^{14}\,{\rm M}_\odot$ and $z = \{0.05, 0.25\}$, respectively), calculated using Eq. (7) in Miller et al. (2016), appropriate for clusters in an expanding universe. This calculation shows that $5r_{200}$ is indeed similar to the turn-around radius,as discussed above. The peculiar velocities of many redMaPPer groups significantly exceed the escape velocity. These objects are not falling into the main clusters, although some of them might be part of the same large-scale structure. CHANCES will enable us to assess the filamentary structure in detail, including embedded groups that are associated with the clusters in our sample. In-depth analyses of the filamentary structure around the CHANCES clusters from the available photometric data will be presented by Baier et al. (in prep.) and Piraino-Cerda et al. (in prep.). Combined with the optical properties of the member galaxies from ancillary imaging and the CHANCES spectra, and combined with X-ray and SZ measurements of the intragroup medium properties (in some cases individually and in some cases through stacking), CHANCES will allow us to closely link the infall history of galaxies that fall into CHANCES clusters as members of groups or as part of the filamentary network but not a group, and also with field galaxies outside this network.

Finally, we show in Fig. 7 the mass function of redMaPPer groups with $|v_{\rm pec}| < 3\sigma_{\rm main}$ (a common first selection of member galaxies within clusters), again taking the richness-derived masses and excluding main CHANCES clusters. We show the mass function in units of the main cluster mass as listed in Tables A.1 and A.2, whereas the masses of infalling groups are the richness-derived masses. As described in Appendix B, the two mass estimates have consistent medians, with a scatter about each other of 0.2−0.3 dex. Interestingly, the Low-z and Evolution populations both follow the same mass distribution for mass ratios $\mu \equiv M_{200}^{\rm infalling}/M_{200}^{\rm main} > 0.03$, preliminarily suggesting a lack of evolution of the high-mass end of the infall mass function over the past 5 Gyr. The most natural interpretation of the abrupt drop at lower mass ratios is that the redMaPPer catalogue is incomplete at low masses: The points at which both distributions turn over correspond approximately to $M_{200}^{\rm infalling} \sim 10^{13}\,{\rm M}_\odot$, in which mass regime the red sequence is not expected to be as dominant as required by redMaPPer.

4.2. Multiple-cluster systems

In addition to the rich array of infalling groups, a few CHANCES clusters are associated with each other: They overlap with other CHANCES clusters on the sky and in redshift. We defined a multiple-cluster system of clusters as a system in which the $5r_{200}$

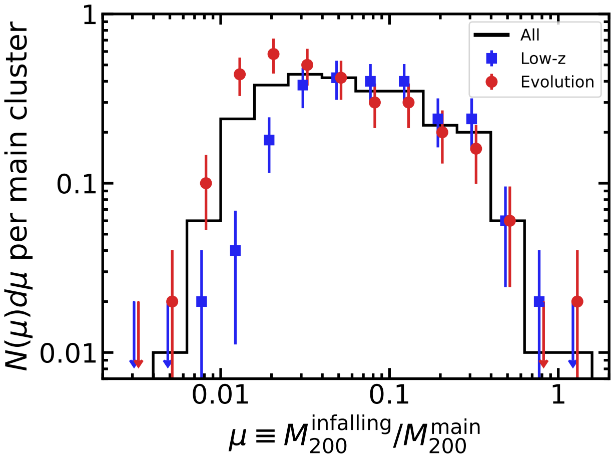

Fig. 7. Mass functions of infalling groups for the Low-z (blue) and Evolution (red) samples and for the two combined (black), including only redMaPPer groups with spectroscopic redshifts and $|v_{\rm pec}| < 3\sigma_{\rm main}$. Differential counts are normalised to the number of CHANCES clusters in each sample and are not corrected for incompleteness. The error bars are Poisson uncertainties, and the arrows are 1σ upper limits. We show the full sample as a histogram and omit the error bars to avoid cluttering. The blue and red data points are slightly shifted horizontally for clarity.

circles of multiple clusters overlap. These systems are listed in Table 3, and they will offer an even larger view of the cosmic web that surrounds massive clusters. They will also serve as an intermediate regime between single CHANCES clusters and superclusters. All of these overlapping systems are part of the Low-z subsurvey, except for Abell 1650/1651.

We show the Abell 3651/3667 system in Figure 8 as an example. Arp & Russell (2001) recognised a possible connection between these two clusters based on the distributions of galaxies in optical images and of X-ray point sources from ROSAT data. Dietl et al. (2024) detected a bridge of X-ray emission that connects these two clusters in the eROSITA X-ray images, which is nicely traced by the structure of redMaPPer groups shown in Fig. 8. Furthermore, like many other CHANCES clusters, Abell 3667 is a well-known merging system with a spectacular morphology at radio wavelengths that traces non-thermal phenomena in the ICM (de Gasperin et al. 2022). In combination with ICM data, CHANCES will reveal the full extent of the network that connects these two clusters and the others in Table 3.

Table 3. Multiple-cluster systems that overlap on the sky and in redshift space.

CHANCES clusters	Redshift
Antlia/Hydra	0.012/0.012
A119/A147/A168	0.044/0.044/0.044
A754/A780	0.054/0.057
A1631/A1644	0.047/0.048
A1650/A1651	0.085/0.085
A2717/A4059	0.050/0.048
A2870/A2877	0.023/0.024
A3651/A3667	0.060/0.053

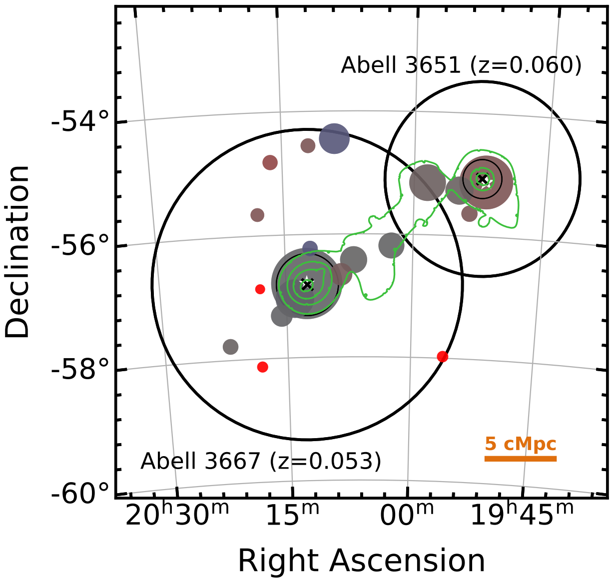

Fig. 8. The Abell 3651/3667 system as an example of overlapping CHANCES clusters (see Sect. 4.2). The symbols and colours are the same as in Fig. 5, but we do not highlight redMaPPer systems according to the CHANCES velocity dispersions. The circle colours are with respect to a reference $z = 0.056$, and the orange bar at the bottom right shows 5 comoving Mpc at the same redshift. The green contours show the eROSITA detection of hot gas within and between the clusters (Dietl et al. 2024).

4.3. Superclusters

We end this sneak peek by showing in Fig. 9 all redMaPPer clusters within and around the two supercluster regions. We illustrate the hierarchy of clusters in each supercluster by defining primary clusters as those that are the most massive system within their $5r_{200}$ and do not lie within the $5r_{200}$ of any more massive cluster. All clusters that are not primaries are labelled as secondary. When we consider only the regions to be surveyed by CHANCES, there are 21 primary and 53 secondary clusters in Shapley and 44 primary and 92 secondary clusters in Horologium-Reticulum. Although we drew full circles around all primary clusters within the survey regions in Fig. 9, only the area within the thick polygons will be observed. The exceptions are the two clusters shown with blue crosses in Fig. 9: Abell 3571 in Shapley, and Abell 3266 in Horologium-Reticulum. In these cases, CHANCES will cover the entire $5r_{200}$ area and add the non-overlapping area to the supercluster coverage. The difficulty of characterising low-redshift structures with photometric redshifts is again highlighted in the lack of a match in the redMaPPer catalogue for Abell 3571: This cluster is at $z = 0.039$, but the only $z < 0.2$ redMaPPer cluster within 20′ has $z_{\rm phot} = 0.19$ and $\lambda = 5$. Evidently, the absence of Abell 3571 from the redMaPPer catalogue affects our census of primary and secondary clusters. This highlights once again the need for CHANCES spectroscopy.

As mentioned in Sect. 2.1.2, Abell 3574 is located just north of Abell 3571, but at $z = 0.016$, it is at a significantly lower redshift than the Shapley supercluster (and Abell 3571). This means that target overlap will be negligible in this case, even though both targets (i.e. Abell 3574 and the Shapley supercluster) overlap in the sky. A similar situation occurs in Horologium-Reticulum, which significantly overlaps the Fornax cluster (whose $5r_{200}$ reaches as far south as $-46°$) on the sky, but not in redshift.

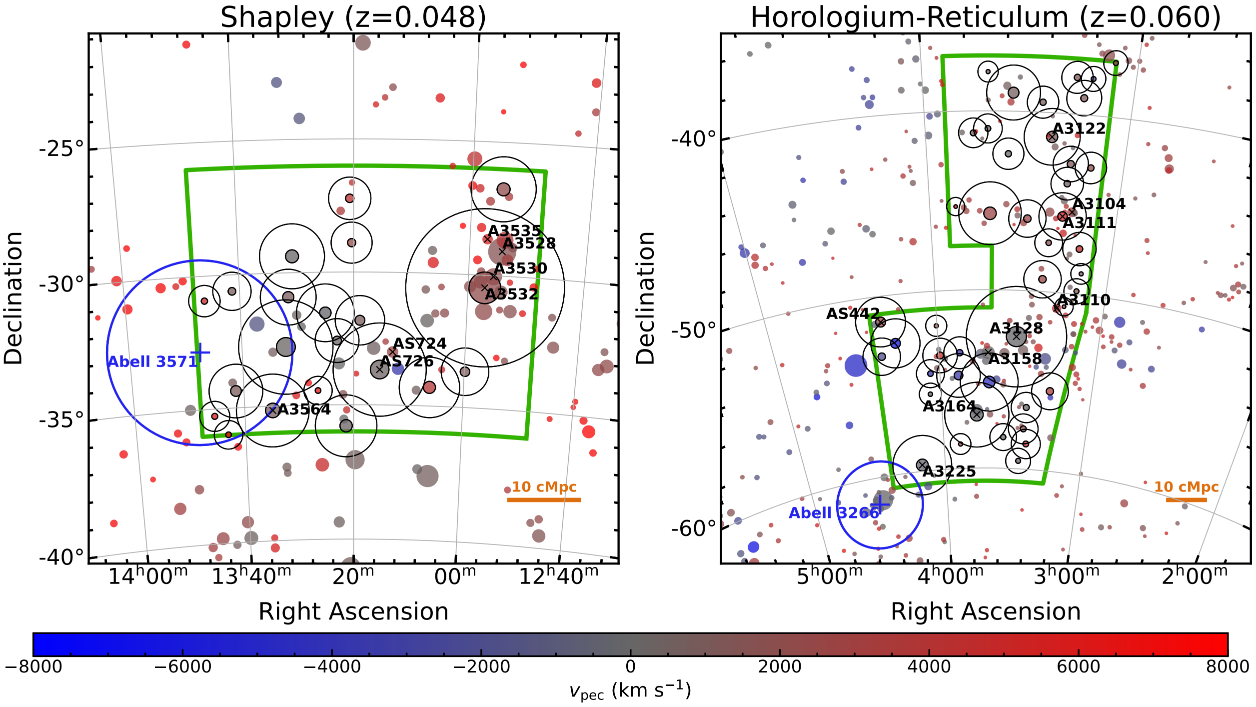

Fig. 9. Optical groups and clusters identified with redMaPPer within and around the Shapley (left) and Horologium-Reticulum (right) superclusters. The colours represent the velocity with respect to the mean supercluster redshift (titles). The sizes are equal to r_{200} determined through the redMaPPer richness. The coloured circles with black outlines are primary clusters (only shown within the supercluster regions), and circles without the black outline are secondary clusters or clusters outside the CHANCES supercluster survey areas, which are marked with green polygons. For primary clusters, we also show $5r_{200}$ with a black circle. The blue crosses and circles mark clusters Abell 3571 (left) and Abell 3266 (right), which are at the supercluster redshifts, but are targeted individually as CHANCES main clusters. We also mark the most massive redMaPPer systems associated with Abell clusters with black crosses (not all of them are primaries).

5. Summary

We presented the cluster sample for CHANCES, the Chilean Cluster galaxy Evolution Survey. This is one of 18 4MOST public surveys that will use the 4MOST Spectroscopic Survey Facility on the VISTA 4m telescope over the next five years. CHANCES will obtain spectra for 500 000 galaxies out to $5r_{200}$ around galaxy clusters at $z < 0.45$ (Fig. 1) in three different regimes that we list below.

(i) $m^\star > 10^{8.5}\,{\rm M}_\odot$ galaxies around 50 clusters at $z < 0.07$, covering an order of magnitude in cluster masses (Fig. 3, left panel).

(ii) $m^\star > 10^{8.5}\,{\rm M}_\odot$ galaxies in large contiguous regions over a total of 353 deg^2, covering the Shapley ($z = 0.048$) and Horologium-Reticulum ($z = 0.060$) superclusters (Fig. 9).

(iii) $m^\star > 10^{10}\,{\rm M}_\odot$ galaxies around 50 of the most massive clusters at $0.07 < z < 0.45$ (Fig. 3, right panel).

Points (i) and (ii) comprise the Low-z subsurvey (Sect. 2.1), and point (iii) refers to the Evolution subsurvey (Sect. 2.2). Clusters in the Low-z subsurvey were selected by combining the AXES-2MRS catalogue (Khalil et al. 2024) at $z < 0.04$ with the WINGS survey at $0.04 < z < 0.07$ (Fasano et al. 2006). The clusters in the Evolution subsurvey were selected as the most massive southern clusters from the second Planck SZ-selected cluster catalogue (Planck Collaboration XXVII 2016) in five bins across $0.07 < z < 0.45$ to ensure uniform redshift coverage. With the exception of the Antlia cluster at $z = 0.0087$, we require multi-band optical imaging from DECaLS DR10 for a uniform photometry and astrometry to select clusters in the two subsurveys.

We produced consistent mass estimates for all clusters by rescaling masses from a number of literature sources (Fig. 2) in order to obtain mass estimates that are consistent with weak lensing measurements from MENeaCS (Herbonnet et al. 2020) and LoCuSS (Okabe & Smith 2016), which in turn are consistent with a number of other weak lensing mass estimates, as well as calibrated SZ-based mass estimates from ACT and SPT.

As a proof of concept for some of the main CHANCES goals, we used the redMaPPer red-sequence catalogue, which we ran on the LSDR10 imaging data to present a preliminary census of groups surrounding the CHANCES clusters (Figs. 5 and 8) as well as the cluster and group distribution composing the CHANCES superclusters (Fig. 9). The reconstructed peculiar velocities suggest that the CHANCES clusters tend to reside in local attractors, although they cover a wide range of large-scale environments. We also presented preliminary measurements of the stacked phase-space (Fig. 6) and mass function (Fig. 7) of groups associated with the CHANCES clusters. The unique wide coverage and high completeness of CHANCES will provide an unprecedented view of the evolution of galaxies and the growth of structure that is facilitated by the cosmic web. Beyond our census of infalling groups, CHANCES will reveal the full extent of the multi-phase cosmic web that surrounds massive clusters, including the sheets and filaments that funnel these groups into their more massive neighbours.

In a series of forthcoming papers, we will present the target selection procedure in detail. It involves assessing cluster membership from photometric data as well as thorough analyses of the substructure and large-scale structure based on the resulting target catalogues.

Data availability

The code used for the analysis and figures in this paper is publicly available at `https://github.com/4MOST-CHANCES/cluster-catalogues`

Acknowledgements. We thank the anonymous referee for their thorough, constructive review, which helped improve the clarity of the paper, and Jakob Dietl for sharing the eROSITA contours for the Abell 3651/3667 system. CS, YJ, RD, AM, and HMH acknowledge support from the Agencia Nacional de Investigación y Desarrollo (ANID) through Basal project FB210003. CS acknowledges support from FONDECYT Iniciación grant no. 11191125. AF thanks FINCA, USM, UdA for the travel support. CPH, YJ, HMH, RBS, DP, FPC, and RS gratefully acknowledge financial support from ANID – MILENIO – NCN2024_112. CPH acknowledges support from ANID through Fondecyt Regular 2021 project no. 1211909. YJ acknowledges support from FONDECYT Regular grants no. 1241426 and 1230441. BMA acknowledges the Universidad de Atacama PhD Scholarship and the Fondecyt Regular 2021 Grant of Dr. Christopher P. Haines, PhD Supervisor, for the expenses to successfully conduct this research. RD gratefully acknowledges support by the ANID BASAL project FB210003. ERVL acknowledges the financial support given by Coordenação de Aperfeiçoamento de Pessoal de Nível Superior (CAPES, grant 88887.470064/2019-00) and Conselho Nacional de Desenvolvimento Científico e Tecnológico (CNPq, grant 169181/2017-0). CL-D acknowledges a grant from the ESO Comite Mixto 2022. HMH acknowledges support from National Fund for Scientific and Technological Research of Chile (FONDECYT) through grant no. 3230176. AM acknowledges support by the FONDECYT Regular grant 1212046 and funding from the Max Planck Society through a “PartnerGroup” grant and the HORIZON-MSCA-2021-SE-01 Research and Innovation Programme under the Marie Sklodowska-Curie grant agreement number 101086388. FA-F acknowledges funding for this work from FAPESP grant 2018/20977-2. PA-A thanks the Coordenaçõ de Aperfeiçoamento de Pessoal de Nível Superior – Brasil (CAPES), for supporting his PhD scholarship (project 88882.332909/2020-01). MA-F acknowledges support from ANID FONDECYT iniciación project 11200107 and the Emergia program (EMERGIA20_38888) from Consejería de Universidad, Investigación e Innovación de la Junta de Andalucía. ANID/Subdirección de Capital Humano/Doctorado Nacional/2023 – 21231017. CRB acknowledges the financial support from CNPq (316072/2021-4) and from FAPERJ (grants 201.456/2022 and 210.330/2022) and the FINEP contract 01.22.0505.00 (ref. 1891/22). HMC acknowledges support from the Institut Universitaire de France and from Centre National d’Etudes Spatiales (CNES), France. GD acknowledges support by UKRI-STFC grants: ST/T003081/1 and ST/X001857/1. AD is supported by a KIAS Individual Grant PG 087201 at the Korea Institute for Advanced Studies. RFH acknowledge financial support from Consejo Nacional de Investigaciones Científicas y Tecnicas (CONICET), Agencia I+D+i (PICT 2019–03299), and Universidad Nacional de La Plata (Argentina). FRH acknowledges support from FAPESP grants 2018/21661-9 and 2021/11345-5. EI acknowledge funding by ANID FONDECYT Regular 1221846. UK acknowledges financial support from the UK Science and Technology Facilities Council (STFC; grant ref: ST/T000171/1). ARL acknowledges financial support from CONICET, Agencia I+D+i (PICT 2019-03299) and Universidad Nacional de La Plata (Argentina). SL acknowledges support by FONDECYT grant 1231187. CMdO acknowledges funding of the S-PLUS project through FAPESP grant 2019/26492-3. LM acknowledge the support from PROYECTOS FONDO de ASTRONOMIA ANID–ALMA 2021 Code: ASTRO21-0007. DP acknowledges financial support from ANID through FONDECYT Postdoctrorado Project 3230379. FPC acknowledges financial support from Dirección de Postgrado (Universidad Técnica Federico Santa María, Chile) through Becas Internas para Doctorado y Magíster Científico-Tecnológicos. AVSC acknowledges financial support from CONICET, Agencia I+D+i (PICT 2019-03299) and Universidad Nacional de La Plata (Argentina). RS acknowledges financial support from FONDECYT Regular 2023 project No. 1230441 LSJ acknowledges the support from CNPq (308994/2021-3) and FAPESP (2011/51680-6). ET was supported by the Estonian Ministry of Education and Research (grant TK202), Estonian Research Council grant (PRG1006) and the European Union’s Horizon Europe research and innovation programme (EXCOSM, grant No. 101159513). This work made use of Astropy: a community-developed core Python package and an ecosystem of tools and resources for astronomy (Astropy Collaboration 2013, 2018, 2022, `http://www.astropy.org`). This work has benefited from open-source software including Matplotlib (Hunter 2007, `https://matplotlib.org/`), NumPy (Harris et al. 2020, `https://numpy.org/`), SciPy (Virtanen et al. 2020, `https://scipy.org/`), and Pandas (The Pandas Development Team 2024, `https://pandas.pydata.org/`). This work has been undertaken in the framework of the 4MOST collaboration (`https://www.4most.eu/cms/home/`).

References

Abell, G. O., Corwin, H. G., & Olowin, R. P. 1989, ApJS, 70, 1
Ade, P., Aguirre, J., Ahmed, Z., et al. 2019, JCAP, 2019, 056
Alberts, S., & Noble, A. 2022, Universe, 8, 554
Anand, A., Nelson, D., & Kauffmann, G. 2021, MNRAS, 504, 65
Andrade-Santos, F., Jones, C., Forman, W. R., et al. 2017, ApJ, 843, 76
Araya-Melo, P. A., Reisenegger, A., Meza, A., et al. 2009, MNRAS, 399, 97
Arp, H., & Russell, D. 2001, ApJ, 549, 802
Astropy Collaboration (Robitaille, T. P., et al.) 2013, A&A, 558, A33
Astropy Collaboration (Price-Whelan, A. M., et al.) 2018, AJ, 156, 123
Astropy Collaboration (Price-Whelan, A. M., et al.) 2022, ApJ, 935, 167
Bahé, Y. M., McCarthy, I. G., Balogh, M. L., & Font, A. S. 2013, MNRAS, 430, 3017
Bahé, Y. M., Schaye, J., Barnes, D. J., et al. 2019, MNRAS, 485, 2287
Bertschinger, E. 1985, ApJS, 58, 39
Bianconi, M., Smith, G. P., Haines, C. P., et al. 2018, MNRAS, 473, L79
Bleem, L. E., Stalder, B., de Haan, T., et al. 2015, ApJS, 216, 27
Bleem, L. E., Bocquet, S., Stalder, B., et al. 2020, ApJS, 247, 25
Böhringer, H., Schuecker, P., Guzzo, L., et al. 2004, A&A, 425, 367
Boselli, A., Fossati, M., & Sun, M. 2022, A&ARv, 30, 3
Brown, T., Catinella, B., Cortese, L., et al. 2017, MNRAS, 466, 1275
Bruzual, G., & Charlot, S. 2003, MNRAS, 344, 1000
Bulbul, E., Liu, A., Kluge, M., et al. 2024, A&A, 685, A106
Butcher, H., & Oemler, A. Jr. 1984, ApJ, 285, 426
Cautun, M., van de Weygaert, R., Jones, B. J. T., & Frenk, C. S. 2014, MNRAS, 441, 2923
Cava, A., Bettoni, D., Poggianti, B. M., et al. 2009, A&A, 495, 707
CCAT-Prime Collaboration (Aravena, M., et al.) 2023, ApJS, 264, 7
Chabrier, G. 2003, PASP, 115, 763
CHEX-MATE Collaboration (Arnaud, M., et al.) 2021, A&A, 650, A104
Clerc, N., Kirkpatrick, C. C., Finoguenov, A., et al. 2020, MNRAS, 497, 3976
Courtois, H. M., Dupuy, A., Guinet, D., et al. 2023, A&A, 670, L15
Damsted, S., Finoguenov, A., Clerc, N., et al. 2023, A&A, 676, A127
Damsted, S., Finoguenov, A., Lietzen, H., et al. 2024, A&A, 690, A52
de Gasperin, F., Rudnick, L., Finoguenov, A., et al. 2022, A&A, 659, A146
de Jong, R. S., Barden, S. C., Bellido-Tirado, O., et al. 2016, SPIE Conf. Ser., 9908, 99081O
de Jong, R. S., Agertz, O., Berbel, A. A., et al. 2019, The Messenger, 175, 3
de Jong, R. S., Bellido-Tirado, O., Brynnel, J. G., et al. 2022, SPIE Conf. Ser., 12184, 1218414
de Vos, K., Merrifield, M. R., & Hatch, N. A. 2024, MNRAS, 531, 4383
Dey, A., Schlegel, D. J., Lang, D., et al. 2019, AJ, 157, 168
Diemer, B. 2018, ApJS, 239, 35
Dietl, J., Pacaud, F., Reiprich, T. H., et al. 2024, A&A, 691, A286
Donnan, C. T., Tojeiro, R., & Kraljic, K. 2022, Nat. Astron., 6, 599
Dünner, R., Araya, P. A., Meza, A., & Reisenegger, A. 2006, MNRAS, 366, 803
Dupuy, A., & Courtois, H. M. 2023, A&A, 678, A176
Ebeling, H., Stephenson, L. N., & Edge, A. C. 2014, ApJ, 781, L40
Einasto, M., Gramann, M., Park, C., et al. 2018, A&A, 620, A149
Fasano, G., Marmo, C., Varela, J., et al. 2006, A&A, 445, 805
Finoguenov, A., Merloni, A., Comparat, J., et al. 2019, The Messenger, 175, 39
Fleenor, M. C., Rose, J. A., Christiansen, W. A., et al. 2005, AJ, 130, 957
Fleenor, M. C., Rose, J. A., Christiansen, W. A., et al. 2006, AJ, 131, 1280
Fujita, Y. 2004, PASJ, 56, 29
Girardi, M., Boschin, W., Mercurio, A., et al. 2024, A&A, 692, A175
Gnedin, O. Y. 2003, ApJ, 582, 141
Gullieuszik, M., Poggianti, B., Fasano, G., et al. 2015, A&A, 581, A41
Gunn, J. E., & Gott, J. R. 1972, ApJ, 176, 1
Haines, C. P., Pereira, M. J., Smith, G. P., et al. 2013, ApJ, 775, 126
Haines, C. P., Pereira, M. J., Smith, G. P., et al. 2015, ApJ, 806, 101
Haines, C. P., Busarello, G., Merluzzi, P., et al. 2018, MNRAS, 481, 1055
Haines, C., Jaffé, Y., Tejos, N., et al. 2023, The Messenger, 190, 31
Harris, C. R., Millman, K. J., van der Walt, S. J., et al. 2020, Nature, 585, 357
Hasan, F., Burchett, J. N., Abeyta, A., et al. 2023, ApJ, 950, 114
Herbonnet, R., Sifón, C., Hoekstra, H., et al. 2020, MNRAS, 497, 4684
Hilton, M., Sifón, C., Naess, S., et al. 2021, ApJS, 253, 3
Hoekstra, H., Mahdavi, A., Babul, A., & Bildfell, C. 2012, MNRAS, 427, 1298
Hou, A., Parker, L. C., & Harris, W. E. 2014, MNRAS, 442, 406
Hunter, J. D. 2007, Comput. Sci. Eng., 9, 90
Ishiyama, T., Prada, F., Klypin, A. A., et al. 2021, MNRAS, 506, 4210
Ivezić, Ž., Kahn, S. M., Tyson, J. A., et al. 2019, ApJ, 873, 111
Jaffé, Y. L., Smith, R., Candlish, G. N., et al. 2015, MNRAS, 448, 1715
Jaffé, Y. L., Verheijen, M. A. W., Haines, C. P., et al. 2016, MNRAS, 461, 1202
Jin, S., Trager, S. C., Dalton, G. B., et al. 2024, MNRAS, 530, 2688
Kesebonye, K. C., Hilton, M., Knowles, K., et al. 2023, MNRAS, 518, 3004
Khalil, H., Finoguenov, A., Tempel, E., & Mamon, G. A. 2024, A&A, 690, A212
Kluge, M., Comparat, J., Liu, A., et al. 2024, A&A, 688, A210

Knuth, K. H. 2006, ArXiv e-prints [arXiv:physics/0605197]
Kriek, M., van Dokkum, P. G., Labbé, I., et al. 2009, ApJ, 700, 221
Kuchner, U., Haggar, R., Aragón-Salamanca, A., et al. 2022, MNRAS, 510, 581
Kugel, R., Schaye, J., Schaller, M., Forouhar Moreno, V. J., & McGibbon, R. J. 2025, MNRAS, 537, 2179
Kulier, A., Poggianti, B., Tonnesen, S., et al. 2023, ApJ, 954, 177
Lima, E. V. R., Sodré, L., Bom, C. R., et al. 2022, Astron. Comput., 38, 100510
Lopes, P. A. A., Ribeiro, A. L. B., & Brambila, D. 2024, MNRAS, 527, L19
Lopez, S., Barrientos, L. F., Lira, P., et al. 2008, ApJ, 679, 1144
Lucey, J. R., Dickens, R. J., Mitchell, R. J., & Dawe, J. A. 1983, MNRAS, 203, 545
Lyke, B. W., Higley, A. N., McLane, J. N., et al. 2020, ApJS, 250, 8
Mamon, G. A., Sanchis, T., Salvador-Solé, E., & Solanes, J. M. 2004, A&A, 414, 445
Martínez, H. J., Muriel, H., & Coenda, V. 2016, MNRAS, 455, 127
McClintock, T., Varga, T. N., Gruen, D., et al. 2019, MNRAS, 482, 1352
McGee, S. L., Balogh, M. L., Bower, R. G., Font, A. S., & McCarthy, I. G. 2009, MNRAS, 400, 937
Mendes de Oliveira, C., Ribeiro, T., Schoenell, W., et al. 2019, MNRAS, 489, 241
Merloni, A., Alexander, D. A., Banerji, M., et al. 2019, The Messenger, 175, 42
Merloni, A., Lamer, G., Liu, T., et al. 2024, A&A, 682, A34
Merluzzi, P., Busarello, G., Haines, C. P., et al. 2015, MNRAS, 446, 803
Miller, C. J., Stark, A., Gifford, D., & Kern, N. 2016, ApJ, 822, 41
Montaguth, G. P., Monachesi, A., Torres-Flores, S., et al. 2025, A&A, 696, A240
Moretti, A., Poggianti, B. M., Fasano, G., et al. 2014, A&A, 564, A138
Moretti, A., Gullieuszik, M., Poggianti, B., et al. 2017, A&A, 599, A81
Munari, E., Biviano, A., Borgani, S., Murante, G., & Fabjan, D. 2013, MNRAS, 430, 2638
Muzzin, A., van der Burg, R. F. J., McGee, S. L., et al. 2014, ApJ, 796, 65
Natarajan, P., Kneib, J.-P., & Smail, I. 2002, ApJ, 580, L11
Navarro, J. F., Frenk, C. S., & White, S. D. M. 1996, ApJ, 462, 563
Okabe, N., & Smith, G. P. 2016, MNRAS, 461, 3794
O'Kane, C. J., Kuchner, U., Gray, M. E., & Aragón-Salamanca, A. 2024, MNRAS, 534, 1682
Oman, K. A., Hudson, M. J., & Behroozi, P. S. 2013, MNRAS, 431, 2307
Pallero, D., Gómez, F. A., Padilla, N. D., et al. 2022, MNRAS, 511, 3210
Piffaretti, R., Arnaud, M., Pratt, G. W., Pointecouteau, E., & Melin, J. B. 2011, A&A, 534, A109
Piraino-Cerda, F., Jaffé, Y. L., Lourenço, A. C., et al. 2024, MNRAS, 528, 919
Pizzardo, M., Geller, M. J., Kenyon, S. J., & Damjanov, I. 2024, A&A, 683, A82
Planck Collaboration XXIV. 2016, A&A, 594, A24
Planck Collaboration XXVII. 2016, A&A, 594, A27
Planck Collaboration VI. 2020, A&A, 641, A6
Proust, D., Quintana, H., Carrasco, E. R., et al. 2006, A&A, 447, 133
Quilis, V., Planelles, S., & Ricciardelli, E. 2017, MNRAS, 469, 80
Raj, M. A., Awad, P., Peletier, R. F., et al. 2024, A&A, 690, A92
Reiprich, T. H., Veronica, A., Pacaud, F., et al. 2021, A&A, 647, A2
Reisenegger, A., Quintana, H., Carrasco, E. R., & Maze, J. 2000, AJ, 120, 523
Rines, K., & Diaferio, A. 2006, AJ, 132, 1275
Rossetti, M., Gastaldello, F., Eckert, D., et al. 2017, MNRAS, 468, 1917
Rozo, E., Bartlett, J. G., Evrard, A. E., & Rykoff, E. S. 2014, MNRAS, 438, 78
Rozo, E., Rykoff, E. S., Abate, A., et al. 2016, MNRAS, 461, 1431
Rykoff, E. S., Rozo, E., Busha, M. T., et al. 2014, ApJ, 785, 104
Sereno, M. 2015, MNRAS, 450, 3665
Sifón, C., & Han, J. 2024, A&A, 686, A163
Smith, R., Choi, H., Lee, J., et al. 2016, ApJ, 833, 109
Smith, R., Calderón-Castillo, P., Shin, J., Raouf, M., & Ko, J. 2022, AJ, 164, 95
Stroe, A., Sobral, D., Paulino-Afonso, A., et al. 2017, MNRAS, 465, 2916
Taylor, E. N., Hopkins, A. M., Baldry, I. K., et al. 2011, MNRAS, 418, 1587
Tempel, E., Tuvikene, T., Kipper, R., & Libeskind, N. I. 2017, A&A, 602, A100
Tempel, E., Kruuse, M., Kipper, R., et al. 2018, A&A, 618, A81
Tempel, E., Tuvikene, T., Muru, M. M., et al. 2020a, MNRAS, 497, 4626
Tempel, E., Norberg, P., Tuvikene, T., et al. 2020b, A&A, 635, A101
The Pandas Development Team 2024, https://doi.org/10.5281/zenodo.3509134
Tollet, É., Cattaneo, A., Mamon, G. A., Moutard, T., & van den Bosch, F. C. 2017, MNRAS, 471, 4170
Treu, T., Ellis, R. S., Kneib, J.-P., et al. 2003, ApJ, 591, 53
Veronica, A., Reiprich, T. H., Pacaud, F., et al. 2024, A&A, 681, A108
Virtanen, P., Gommers, R., Oliphant, T. E., et al. 2020, Nat. Meth., 17, 261
Wilman, D. J., Oemler, A., Mulchaey, J. S., et al. 2009, ApJ, 692, 298
Zabludoff, A. I., Zaritsky, D., Lin, H., et al. 1996, ApJ, 466, 104

---

[1] Instituto de Física, Pontificia Universidad Católica de Valparaíso, Casilla 4059, Valparaíso, Chile
[2] Department of Physics, University of Helsinki, Gustaf Hällströmin katu 2, 00560 Helsinki, Finland
[3] Instituto de Astronomía y Ciencias Planetarias (INCT), Universidad de Atacama, Copayapu 485, Copiapó, Chile
[4] Departamento de Física, Universidad Técnica Federico Santa María, Avenida España 1680, Valparaíso, Chile
[5] Institute of Astrophysics, Facultad de Ciencias Exactas, Universidad Andrés Bello, Sede Concepción, Talcahuano, Chile
[6] Departamento de Astronomia, Instituto de Astronomia, Geofísica e Ciências Atmosféricas, Universidade de São Paulo, Rua do Matão 1226, Cidade Universitária, São Paulo 05508-090, Brazil
[7] Departamento de Astronomía, Universidad de La Serena, Avda. Raúl Bitrán 1305, La Serena, Chile
[8] Instituto Multidisciplinario de Investigación y Postgrado, Raúl Bitrán, 1305 La Serena, Chile
[9] INAF – Osservatorio Astronomico di Capodimonte, Salita Moiariello 16, 80131 Napoli, Italy
[10] Centro Brasileiro de Pesquisas Físicas, Rua Dr. Xavier Sigaud 150, 22290-180 Rio de Janeiro, RJ, Brazil
[11] Observatório do Valongo, Ladeira Pedro Antônio, 43, Saúde, Rio de Janeiro 20080-090, BR, Brazil
[12] Departamento de Física Teórica y del Cosmos, Edificio Mecenas, Campus Fuentenueva, Universidad de Granada, E-18071 Granada, Spain
[13] Instituto Universitario Carlos I de Física Teórica y Computacional, Universidad de Granada, 18071 Granada, Spain
[14] Instituto de Física y Astronomía, Universidad de Valparaíso, Avda. Gran Bretaña 1111, Valparaíso, Chile
[15] Centre of Excellence for Data Science, Artificial Intelligence & Modelling, The University of Hull, Cottingham Road, Kingston-Upon-Hull HU6 7RX, UK
[16] Consejo Nacional de Investigaciones Científicas y Técnicas, Ciudad Autónoma de Buenos Aires, Argentina
[17] Instituto de Astrofísica de La Plata, CONICET-UNLP, Paseo del Bosque s/n, B1900FWA La Plata, Argentina
[18] Facultad de Ciencias Astronómicas y Geofísicas, Universidad Nacional de La Plata, Paseo del Bosque s/n, B1900FWA La Plata, Argentina
[19] INAF-IASF Milano, Via Alfonso Corti 12, 20133 Milano, Italy
[20] Max-Planck-Institut für Extraterrestrische Physik (MPE), Gießenbachstraße 1, D-85748 Garching bei München, Germany
[21] Université Claude Bernard Lyon 1, IUF, IP2I Lyon, 4 Rue Enrico Fermi, 69622 Villeurbanne, France
[22] Institute of Astronomy, University of Cambridge, Madingley Road, Cambridge CB3 0HA, United Kingdom
[23] Korea Institute for Advanced Study, 85, Hoegi-ro, Dongdaemun-gu, Seoul 02455, Republic of Korea
[24] Kuffner Observatory, Johann-Staud-Straße 10, 1160 Wien, Austria
[25] CASU, Institute of Astronomy, Cambridge, UK
[26] School of Physics, Astronomy, University of Nottingham, Nottingham NG7 2RD, UK
[27] Departamento de Astronomía, Universidad de Chile, Casilla 36-D, Santiago, Chile
[28] School of Physics and Astronomy, University of Birmingham, Birmingham B15 2TT, UK
[29] INAF-Padova Astronomical Observatory, Vicolo dell'Osservatorio 5, I-35122 Padova, Italy
[30] European Southern Observatory, Science Operations, Alonso de Cordova 3107, Vitacura, 19001 Santiago, Chile
[31] Tartu Observatory, University of Tartu, Observatooriumi 1, Tõravere 61602, Estonia
[32] Estonian Academy of Sciences, Kohtu 6, 10130 Tallinn, Estonia
[33] Millennium Nucleus for Galaxies (MINGAL), Valparaíso, Chile

Appendix A: CHANCES cluster samples

Tables A.1 and A.2 list the CHANCES cluster samples for the Low-z and Evolution subsurveys, respectively, along with the mass estimates and corresponding r_{200}. All of these clusters will be observed out to $5r_{200}$ with the 4MOST spectrograph through the five-year duration of the CHANCES survey.

Table A.1. CHANCES Low-z cluster sample.

(1) Cluster name	(2) RA hh:mm:ss	(3) Dec dd:mm:ss	(4) Redshift	(5) M_{200} $10^{14}\,\mathrm{M}_\odot$	(6) r_{200} Mpc	(7) θ_{200} arcmin	(8) Mass source
Abell 85	00:41:49.9	−09:18:07.2	0.056	8.4	1.96	29.00	MENeaCS
Abell 119	00:56:16.1	−01:15:18.0	0.044	7.8	1.92	35.63	MENeaCS
Abell 133	01:02:41.8	−21:52:55.2	0.057	4.1	1.54	22.45	MENeaCS
Abell 147	01:08:11.5	+02:10:33.6	0.044	1.4	1.08	20.10	MCXC
Abell 151	01:08:50.9	−15:24:25.2	0.053	2.5	1.30	20.28	MCXC
Abell 168	01:15:02.4	+00:18:54.0	0.044	2.4	1.29	24.04	MCXC
Abell 194	01:25:50.4	−01:24:07.2	0.017	0.6	0.83	38.79	AXES-2MRS
Abell 496	04:33:38.4	−13:15:32.4	0.034	5.7	1.73	41.61	AXES-2MRS
Abell 500	04:38:51.8	−22:06:00.0	0.067	3.0	1.37	17.26	MCXC
Abell 548	05:48:29.0	−25:28:58.8	0.041	2.7	1.34	26.63	MCXC
Abell 754	09:08:31.9	−09:36:57.6	0.054	14.9	2.37	36.33	MENeaCS
Abell 780	09:18:06.0	−12:04:58.8	0.057	6.5	1.80	26.20	MENeaCS
Abell 957	10:13:37.9	−00:54:57.6	0.045	2.2	1.25	22.83	MCXC
Abell 970	10:17:33.8	−10:39:57.6	0.059	3.6	1.48	20.85	MCXC
Abell 1069	10:39:43.0	−08:40:58.8	0.062	1.5	1.10	14.79	WINGS
Abell 1520	12:19:19.7	−13:15:36.0	0.068	3.7	1.48	18.29	MCXC
Abell 1631	12:52:51.8	−15:24:00.0	0.047	2.4	1.29	22.59	WINGS
Abell 1644	12:57:10.8	−17:24:00.0	0.048	6.0	1.76	30.11	WINGS
Abell 2399	21:57:22.1	−07:48:39.6	0.058	3.4	1.44	20.67	WINGS
Abell 2415	22:05:39.4	−05:35:38.4	0.058	1.5	1.11	15.87	WINGS
Abell 2457	22:35:40.8	+01:30:21.6	0.058	2.0	1.22	17.47	WINGS
Abell 2717	00:03:13.0	−35:55:58.8	0.050	1.4	1.09	17.93	WINGS
Abell 2734	00:11:20.6	−28:51:18.0	0.061	2.4	1.28	17.56	WINGS
Abell 2870	01:07:43.9	−46:54:00.0	0.023	4.5	1.59	55.14	CODEX
Abell 2877	01:10:00.2	−45:55:22.8	0.024	1.2	1.05	34.83	AXES-2MRS
Abell 3223	04:08:16.1	−30:53:38.4	0.060	3.0	1.38	19.25	MCXC
Abell 3266	04:31:13.0	−61:27:00.0	0.054	7.0	1.84	28.21	SPT-SZ
Abell 3301	05:00:46.6	−38:40:40.8	0.054	2.4	1.30	19.89	MCXC
Abell 3341	05:25:34.1	−31:35:42.0	0.037	1.9	1.20	25.96	AXES-2MRS
Abell 3376	06:00:40.8	−40:01:58.8	0.046	4.0	1.53	27.36	WINGS
Abell 3391	06:26:22.8	−53:41:49.2	0.051	4.3	1.56	25.32	MCXC
Abell 3395	06:27:36.0	−54:25:58.8	0.050	5.1	1.65	27.28	PSZ2
Abell 3490	11:45:19.9	−34:19:58.8	0.069	3.0	1.38	16.91	AXES-LEGACY
Abell 3497	12:00:03.8	−31:22:58.8	0.068	3.1	1.39	17.22	WINGS
Abell 3565	13:36:39.1	−33:57:31.2	0.013	0.2	0.60	36.67	MCXC
Abell 3571	13:47:28.3	−32:50:56.4	0.039	8.7	1.99	41.49	AXES-2MRS
Abell 3574	13:49:06.7	−30:19:33.6	0.016	2.7	1.36	67.25	AXES-2MRS
Abell 3581	14:07:28.1	−27:00:54.0	0.023	2.0	1.23	42.74	AXES-2MRS
Abell 3651	19:52:16.3	−55:03:43.2	0.060	2.9	1.37	19.01	MCXC
Abell 3667	20:12:26.9	−56:48:57.6	0.053	8.2	1.94	30.28	ACT-DR5
Abell 3716	20:51:30.0	−52:42:57.6	0.045	4.5	1.60	29.12	WINGS
Abell 3809	21:46:58.8	−43:52:58.8	0.063	1.0	0.97	12.85	WINGS
Abell 4059	23:57:00.0	−34:45:32.4	0.048	6.2	1.77	30.28	ACT-DR5
Abell S560	06:00:48.2	−58:35:13.2	0.037	0.8	0.91	19.90	AXES-2MRS
Antlia	10:30:03.4	−35:19:22.8	0.009	1.3	1.06	92.08	PSZ2
Fornax	03:38:27.8	−35:26:52.8	0.005	0.3	0.69	107.25	MCXC
Hydra (A1060)	10:36:41.8	−27:31:26.4	0.012	2.2	1.26	82.82	AXES-2MRS
IIZw108	21:13:55.9	+02:33:54.0	0.048	1.5	1.11	19.09	WINGS
MKW4	12:04:27.6	+01:53:42.0	0.020	1.4	1.08	42.82	AXES-2MRS
MKW8	14:40:42.2	+03:28:19.2	0.027	1.4	1.09	32.46	AXES-2MRS

Notes. Clusters which are part of the Shapely and Horologium-Reticulum superclusters, which are also part of the Low-z survey, are not included in this table. Columns are: (1) literature cluster name; (2) and (3): right ascension and declination corresponding to the adopted cluster centre; (4): literature cluster redshift; (5) and (6): mass and corresponding radius enclosing a mean density of 200 times the critical mass density of the Universe at the cluster redshift; (7) cluster angular size, $\theta_{200} = r_{200}/D_\mathrm{A}$, where D_A is the angular diameter distance; and (8) catalogue from which we take the cluster mass, after normalizing the published masses as discussed in Sect. 3.

Table A.2. CHANCES Evolution sample.

Cluster name	RA hh:mm:ss	Dec dd:mm:ss	Redshift 10^{14} $M_\odot$	M_{200} Mpc	r_{200} arcmin	θ_{200}	Mass source
Abell 209	01:31:53.5	−13:36:46.8	0.209	8.5	1.86	8.80	MENeaCS
Abell 370	02:39:50.4	−01:35:06.0	0.373	24.1	2.47	7.76	MENeaCS
Abell 520	04:54:06.5	+02:57:43.2	0.203	11.5	2.07	9.99	MENeaCS
Abell 521	04:54:09.1	−10:14:20.4	0.247	5.8	1.62	6.74	LoCuSS
Abell 1300	11:31:54.5	−19:55:40.8	0.306	12.5	2.04	7.29	SPT-ECS
Abell 1437	12:00:26.2	+03:20:52.8	0.134	3.9	1.48	10.03	CoMaLit
Abell 1650	12:58:42.0	−01:45:32.4	0.085	10.5	2.09	21.21	MENeaCS
Abell 1651	12:59:28.1	−04:12:03.6	0.085	8.3	1.93	19.60	MENeaCS
Abell 1689	13:11:30.0	−01:20:06.0	0.183	11.4	2.07	10.86	LoCuSS
Abell 1835	14:00:52.3	+02:52:40.8	0.252	10.5	1.96	8.06	LoCuSS
Abell 2163	16:15:49.2	−06:09:07.2	0.206	13.1	2.15	10.30	MENeaCS
Abell 2420	22:10:16.6	−12:10:37.2	0.085	8.4	1.94	19.58	MENeaCS
Abell 2744	00:14:18.7	−30:23:20.4	0.308	20.6	2.41	8.58	CoMaLit
Abell 2811	00:42:08.6	−28:32:09.6	0.108	6.2	1.74	14.22	CoMaLit
Abell 2813	00:43:27.8	−20:37:01.2	0.292	8.5	1.80	6.66	LoCuSS
Abell 3048	02:46:27.6	−20:32:06.0	0.310	8.2	1.77	6.27	ACT-DR5
Abell 3186	03:52:14.6	−74:00:28.8	0.127	10.2	2.03	14.44	PSZ2
Abell 3378	06:05:52.6	−35:18:32.4	0.139	8.8	1.93	12.70	PSZ2
Abell 3404	06:45:29.3	−54:13:08.4	0.164	16.0	2.33	13.34	ACT-DR5
Abell 3444	10:23:50.9	−27:15:32.4	0.254	11.5	2.02	8.25	SPT-ECS
Abell 3695	20:34:49.4	−35:49:30.0	0.089	7.5	1.87	18.10	CoMaLit
Abell 3822	21:54:06.7	−57:51:46.8	0.076	5.3	1.67	18.68	ACT-DR5
Abell 3827	22:01:52.6	−59:56:20.4	0.098	12.5	2.20	19.62	ACT-DR5
Abell 3911	22:46:17.0	−52:43:19.2	0.097	6.7	1.79	16.11	PSZ2
Abell 3921	22:49:49.4	−64:24:54.0	0.094	7.0	1.82	16.77	SPT-SZ
Abell S780	14:59:29.3	−18:11:13.2	0.236	12.3	2.08	8.98	PSZ2
Bullet	06:58:31.0	−55:56:49.2	0.296	14.3	2.14	7.83	CoMaLit
MACS J0329.7−0211	03:29:41.5	−02:11:45.6	0.450	8.6	1.70	4.78	CoMaLit
MACS J0416.1−2403	04:16:09.8	−24:03:57.6	0.397	10.7	1.87	5.65	CoMaLit
MACS J0553.4−3342	05:53:27.1	−33:42:54.0	0.430	21.4	2.34	6.75	ACT-DR5
MACS J1206.2−0847	12:06:12.2	−08:48:00.0	0.441	18.1	2.19	6.22	CoMaLit
PSZ2 G205.93−39.64	04:17:37.4	−11:53:45.6	0.443	30.6	2.61	7.38	CoMaLit
PSZ2 G208.60−26.00	05:10:47.8	−08:01:44.4	0.219	13.0	2.14	9.74	ACT-DR5
PSZ2 G241.11−28.68	05:42:57.1	−35:59:02.4	0.420	10.0	1.82	5.32	ACT-DR5
PSZ2 G241.76−30.88	05:32:56.0	−37:01:34.0	0.275	14.7	2.18	8.40	ACT-DR5
PSZ2 G259.98−63.43	02:32:18.7	−44:20:42.0	0.284	17.3	2.29	8.63	ACT-DR5
PSZ2 G262.27−35.38	05:16:36.7	−54:31:12.0	0.295	9.5	1.87	6.86	CoMaLit
PSZ2 G262.73−40.92	04:38:19.0	−54:19:04.8	0.421	15.0	2.07	6.05	ACT-DR5
PSZ2 G271.18−30.95	05:49:18.2	−62:04:58.8	0.376	16.4	2.18	6.80	SPT-SZ
PSZ2 G277.76−51.74	02:54:23.0	−58:57:50.4	0.438	11.2	1.87	5.33	ACT-DR5
PSZ2 G286.98+32.90	11:50:49.2	−28:04:37.2	0.390	31.0	2.67	8.17	CoMaLit
PSZ2 G348.90−67.37	23:25:13.0	−41:12:28.8	0.358	10.9	1.91	6.15	ACT-DR5
RXC J0528.9−3827	05:28:53.0	−39:28:15.5	0.284	12.8	2.07	7.81	ACT-DR5
RXC J1314.4−2515	13:14:28.1	−25:15:39.6	0.244	13.8	2.16	9.06	SPT-ECS
RXC J1347.5−1144	13:47:30.5	−11:45:10.8	0.452	16.1	2.10	5.88	MENeaCS
RXC J1514.9−1523	15:14:58.1	−15:23:09.6	0.223	13.8	2.18	9.81	PSZ2
RXC J2031.8−4037	20:31:51.6	−40:37:15.6	0.341	14.7	2.13	7.07	ACT-DR5
RXC J2211.7−0350	22:11:43.4	−03:49:44.4	0.397	19.4	2.28	6.89	CoMaLit
RXC J2248.7−4431	22:48:43.4	−44:31:44.4	0.347	18.7	2.30	7.55	CoMaLit
SMACS J0723.3−7327	07:23:21.4	−73:26:20.4	0.390	12.8	1.99	6.09	PSZ2

Notes. Columns are as in Table A.1.

Appendix B: Properties of redMaPPer groups

Here we describe the calculation of the properties of redMaPPer groups used in Sect. 4.

The redMaPPer catalogue constructed by Kluge et al. (2024) reports the redshift for each group as derived from one of three techniques: `cg_spec_z`, when the cluster redshift is equal to the central galaxy's spectroscopic redshift; `spec_z_boot`, bootstrapped from multiple (at least three) available spectroscopic redshifts; and `photo_z`, photometric redshifts from the multi-colour red sequence as derived by Rykoff et al. (2014). Uncertainties for the latter two are taken from the redMaPPer catalogue directly.

Uncertainties δz for groups with `cg_spec_z` redshifts are calculated as

$$\delta z = \left[(\delta z_{\rm cg})^2 + (\sigma_v)^2\right]^{1/2}, \tag{B.1}$$

where $\delta z_{\rm cg}$ is the uncertainty in the central galaxy redshift (equal to the reported group redshift uncertainty) and σ_v is the velocity dispersion.

Of the 320 redMaPPer groups within $5r_{200}$ of CHANCES Low-z clusters, there are 90 (28%) with `cg_spec_z`, 161 (50%) with `spec_z_boot`), and 69 (22%) `photo_z`. Typical uncertainties for each set are (250–400, 100–1200, 2800–4600) km s^{-1}, respectively. In the Evolution sample there are a total of 1075 groups within $5r_{200}$ of CHANCES clusters: (86, 157, 832) groups, corresponding to (8%, 15%, 77%), with (`cg_spec_z`, `spec_z_boot`, `photo_z`) and typical uncertainties (300–500, 150–900, 1700–4000) km s^{-1}, respectively. These all correspond to 16th–84th percentile ranges on the uncertainties.

We calculate the peculiar velocity of each redMaPPer group as

$$v_{\rm pec} = \frac{c(z - z_{\rm cl})}{1 + z_{\rm cl}}, \tag{B.2}$$

where z is the redshift reported in the redMaPPer catalogue and $z_{\rm cl}$ is the redshift of the associated CHANCES cluster, as listed in Tables A.1 and A.2. The uncertainty on the peculiar velocity is then $\delta v_{\rm pec} = c[\delta z/(1 + z_{\rm cl})]$.

In order to estimate group masses, M_{200}, we multiply the reported richness, λ, by 1.21 to match the DES richness scale as described by Kluge et al. (2024) and use the relation between λ and weak lensing mass derived by McClintock et al. (2019) for DES clusters. We convert from $M_{\rm 200m}$ (with respect to the mean matter density), estimated from the McClintock et al. (2019) relation, to M_{200} (with respect to the critical matter density) using the mass-concentration relation of Ishiyama et al. (2021) as implemented in `colossus` (Diemer 2018).

Finally, we compare the richness-derived masses with the masses listed in Tables A.1 and A.2, since we combine the two to calculate the infall mass function (Fig. 7). For the Low-z clusters we find a median logarithmic difference $\langle \log M_{200}^{\rm group} - \log M_{200}^{\rm main} \rangle = 0.02$ dex and a 16–84th percentile range $[-0.47, 0.26]$ dex; that is, typically richness-derived masses are between 34% and 182% of the nominal CHANCES masses. Similarly, for Evolution clusters we find a median of -0.07 dex and a 16–84th percentile range $[-0.23, 0.18]$ dex. That is, richness-derived masses are typically between 66% and 151% the nominal CHANCES masses. Although the scatter between the two mass estimates is large, particularly in the case of Low-z, they are statistically consistent with each other.